



Originally published as:

Meqbel, N., Weckmann, U., Muñoz, G., Ritter, O. (2016): Crustal metamorphic fluid flux beneath the Dead Sea Basin: constraints from 2-D and 3-D magnetotelluric modelling. - *Geophysical Journal International*, 207, pp. 1609—1629.

DOI: <http://doi.org/10.1093/gji/ggw359>

Crustal metamorphic fluid flux beneath the Dead Sea Basin: constraints from 2-D and 3-D magnetotelluric modelling

Naser Meqbel,¹ Ute Weckmann,¹ Gerard Muñoz¹ and Oliver Ritter^{1,2}

¹Helmholtz Centre Potsdam GFZ German Research Centre for Geosciences, D-14473 Potsdam, Germany. E-mail: meqbel@gfz-potsdam.de

²Institute of Geophysics, Freie Universität Berlin, Malteserstr. 74-100, D-12249 Berlin, Germany

Accepted 2016 September 26. Received 2016 September 21; in original form 2016 February 17

SUMMARY

We report on a study to explore the deep electrical conductivity structure of the Dead Sea Basin (DSB) using magnetotelluric (MT) data collected along a transect across the DSB where the left lateral strike-slip Dead Sea transform (DST) fault splits into two fault strands forming one of the largest pull-apart basins of the world. A very pronounced feature of our 2-D inversion model is a deep, subvertical conductive zone beneath the DSB. The conductor extends through the entire crust and is sandwiched between highly resistive structures associated with Precambrian rocks of the basin flanks. The high electrical conductivity could be attributed to fluids released by dehydration of the uppermost mantle beneath the DSB, possibly in combination with fluids released by mid- to low-grade metamorphism in the lower crust and generation of hydrous minerals in the middle crust through retrograde metamorphism. Similar high conductivity zones associated with fluids have been reported from other large fault systems. The presence of fluids and hydrous minerals in the middle and lower crust could explain the required low friction coefficient of the DST along the eastern boundary of the DSB and the high subsidence rate of basin sediments. 3-D inversion models confirm the existence of a subvertical high conductivity structure underneath the DSB but its expression is far less pronounced. Instead, the 3-D inversion model suggests a deepening of the conductive DSB sediments off-profile towards the south, reaching a maximum depth of approximately 12 km, which is consistent with other geophysical observations. At shallower levels, the 3-D inversion model reveals salt diapirism as an upwelling of highly resistive structures, localized underneath the Al-Lisan Peninsula. The 3-D model furthermore contains an E–W elongated conductive structure to the northeast of the DSB. More MT data with better spatial coverage are required, however, to fully constrain the robustness of the above-mentioned off-profile features.

Key words: Electrical properties; Magnetotellurics; Transform faults; Crustal structure.

1 INTRODUCTION

The Dead Sea transform (DST) fault extends from the Red Sea spreading centre in the south to the Taurus–Zagros continental collision zone in the north (Fig. 1a); the fault separates the Sinai plate in the west from the Arabian plate in the east with a total length of approximately 1000 km (Garfunkel 1981). As a consequence of continental breakup, the Red Sea and the Gulf of Suez were formed (Garfunkel 1981). Along the DST, the movement partitioned into two main stages (Zak & Freund 1981): an earlier shear movement of 60–65 km took place between 25 and 14 Myr. and a slip of 40–45 km is associated with the last 4.5 Myr. The displacement of older geological formations, particularly from the late Cretaceous, suggests a total displacement of 100–110 km (Garfunkel *et al.* 1981; Zak & Freund 1981). Garfunkel *et al.* (1981) estimated an average slip rate of 7–10 mm yr⁻¹ for the last 4–5 Myr. Based on geomor-

phologic studies carried out in the northern part of the Araba valley (a segment of the DST between the Dead Sea and the Gulf of Aqaba; see Fig. 1a), Klinger *et al.* (2000) suggested an average slip rate of about 4 mm yr⁻¹. Global Position System measurements (Leloup *et al.* 1999) carried out in the Araba valley estimated a present-day slip rate of 4.9 ± 1.4 mm yr⁻¹.

For the later phases of the movement along the fault, Garfunkel *et al.* (1981) suggested oblique shear directions of approximately N15°E which caused the formation of several pull-apart basins. One of them is the Dead Sea basin (DSB), which is approximately 150 km long and extends from the southern Jordan valley near Jericho to the northern segment of the Araba valley (Fig. 1b). The northern part of the basin hosts the Dead Sea; one of the world's most saline lakes containing more than 30 per cent dissolved salts (Neev & Hall 1979). North and south of the lake, the valley floor is 300–400 m

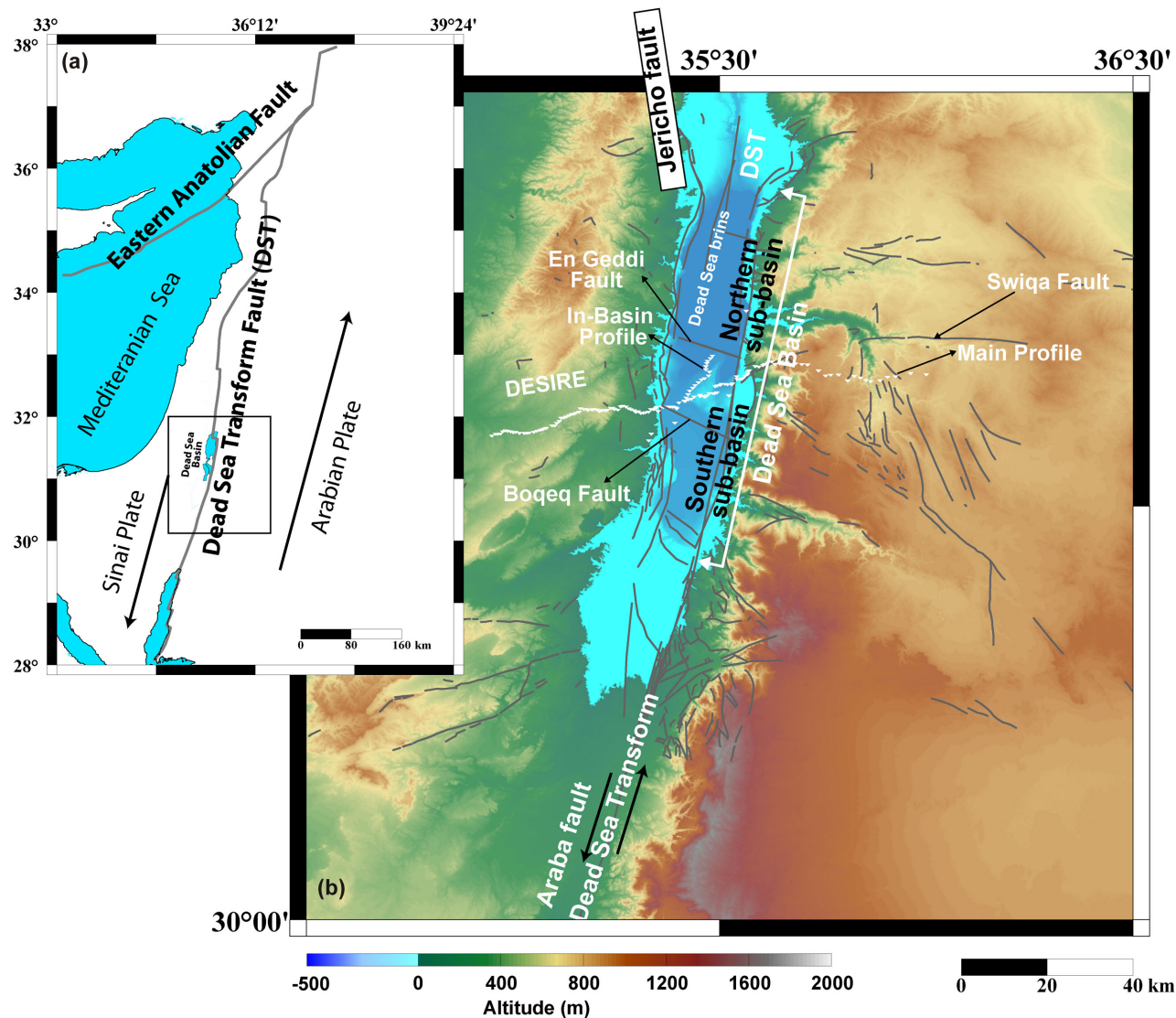


Figure 1. (a) Regional overview map showing the N–S extend of the left lateral strike-slip Dead Sea Transform fault (DST) which separates the Sinai tectonic Plate in the west from the Arabian Plate in the east. (b) Location map with the 151 magnetotelluric sites along the main and in-basin profiles marked as white triangles. Also shown are major faults in the vicinity on the Dead Sea Basin (DSB).

below sea level, while the bottom of the lake is more than 700 m below sea level.

The Araba fault is the expression of the DST south of the DSB, while the fault's north-westward extension is called Jericho fault; both faults are arranged in en-echelon (pull-apart). The DSB is delimited by fault scarps trending in north–south direction but the western fault scarp become weakly expressed at surface towards the northern Araba valley. The DSB is separated by the Al-Lisan Peninsula into northern and southern sub-basins (Garfunkel 1981; Ben-Avraham & Schubert 2006; Ben-Avraham *et al.* 2008).

In the framework of the multinational and interdisciplinary projects DESERT (Dead Sea Rift Transect; Weber *et al.* 2009) and DESIRE (Dead Sea Integrated Research; this study; Weber *et al.* 2011), several geophysical experiments were conducted across the Dead Sea Fault system. From 2-D P -wave velocity models obtained from seismic wide-angle refraction/reflection data across the DST, Mechie *et al.* (2009) suggested depths for the top of the seismic basement (P -wave velocities greater than 5.6 km s^{-1}) of approximately 2 km in the vicinity of the DSB and of approximately 6 km

at the eastern and western ends of the seismic profile. The top of the seismic basement of the southern sub-basin of the DSB was found at a depth of 11 km. Mechie *et al.* (2009) suggested that the Dead Sea pull-apart basin is essentially an upper crustal feature.

Density models derived from gravity data (Ten Brink *et al.* 1993) suggest a sedimentary infill of approximately 9 km for the northern part of the DSB. The largest negative gravity anomaly is associated with the Al-Lisan Peninsula. The gravity low was interpreted as the region of maximum sedimentary fill in excess of 18 km (Ten Brink *et al.* 1993). Other density modelling studies carried out in the framework of DESIRE project suggest a smaller volume of sedimentary basin infill. Choi *et al.* (2011) estimated a thickness of 14 km in the vicinity of the Al-Lisan Peninsula, and thicknesses of approximately 8 km towards the northern and southern sub-basins. The Al-Lisan and Sedom salt diapirs appear as pronounced features in both mentioned density studies.

An integrated investigation by Ben-Avraham & Schubert (2006) and Ben-Avraham *et al.* (2008), with results from Ginzburg &

Ben-Avraham (1997) and Al-Zoubi & Avraham (2002), proposed a sedimentary thickness of approximately 6–8 km for the northern sub-basin. South of the Al-Lisan Peninsula, an SE–NW oriented major normal fault was detected (Boqeq Fault; Fig. 1). Across the Boqeq fault basement overlying sediments to the south are offset by approximately 4–5 km. Hence, the Boqeq fault appears to be the northern boundary of the southern sub-basin which has a sedimentary thickness of ~12 km (Ben-Avraham & Schubert 2006).

Thermomechanic modelling by Sobolev *et al.* (2005) suggested that shear deformation is localized in a 20–40 km wide zone around the DST, with the resulting mechanically weak decoupling zone extending subvertically through the entire lithosphere. Petrunin *et al.* (2012) showed that the DSB can be considered as a classical pull-apart basin, assuming that the lithosphere was thermally eroded at about 20 Myr. and an uppermost mantle with relatively weak rheology, which would be consistent with lab data for wet olivine or pyroxenite.

Electrical and electromagnetic techniques (e.g. TEM and DC geo-electric) have been applied on either side of the rift valley to investigate the hydrological system, particularly to delineate the saline/fresh water interface close to the Dead Sea (Kafri *et al.* 1997; Salameh & E.-Naser 2000; Yechieli *et al.* 2001; Kafri & Goldman 2005; Yechieli 2006; Meqbel *et al.* 2013). Deep magnetotelluric (MT) sounding data were collected in the framework of DESERT project along a long and several shorter profiles across the DST (Araba fault), approximately 150 km to the south of the DSB (Ritter *et al.* 2003). Ritter *et al.* (2003) argued that the shear zone at this particular location of the Araba fault may be exceptionally narrow (in the range of a few metres), beyond the lateral resolution threshold of MT measurements. Instead, the inversion models were indicative for a fault acting as an impermeable barrier for cross-fault fluid transport. Clearly, the strike-slip configuration at this segment of the DST (Araba fault) is in stark contrast to the state of the fault at the DSB, where we observe very significant extensional forces which cause forking of the DST into two fault strands and formation of a very large pull-apart basin (Garfunkel *et al.* 1981; Garfunkel 1981).

In this study, we discuss 2-D and 3-D electrical conductivity models derived from MT data collected in the framework of DESIRE project. The uppermost crustal structures (<4 km) were discussed extensively in Meqbel *et al.* (2013). Here, we focus on implications for the lower crust and mantle lithosphere.

2 MT DATA COLLECTION AND ANALYSIS

The MT data were collected in 2006 October and November; the main profile, approximately 110 km long, was oriented N70° E, approximately perpendicular to the surface trace of the DST. A second, approximately 20 km long ‘in-basin’ profile, was oriented N20° E, roughly parallel to the western shore of the Al-Lisan Peninsula (Fig. 1).

In total, 151 MT stations were deployed with site spacings varying between 0.5 and 2 km. The main profile consisted of 94 sites and the in-basin profile of 59. In the DSB and its vicinity, the site spacing was 0.5 km, further away from the DSB and towards the outer segments of the profile, the distances between the stations increased to 2 km. Short-period automatic magnetotelluric systems (S.P.A.M. MKIII; Ritter *et al.* 1998) and Earth data loggers were used to record data in the frequency range from 1 kHz to 1 mHz. Induction coil magnetometers (Metronix MFS05/6) were used to

record three orthogonal magnetic field components; the horizontal electric fields were measured with non-polarisable Ag/AgCl electrodes of the Geophysical Instrument Pool Potsdam. Data acquisition was accomplished with two independent teams, working at the same time in Jordan and Israel which allowed us to record with up to 30 instruments simultaneously. This provided great flexibility for remote reference processing with many possible station combinations which improved data quality considerably, particularly in the period band 1–10 s. All data were processed with the EMERALD package (Ritter *et al.* 1998; Weckmann *et al.* 2005; Krings 2007) to calculate MT impedance tensors and vertical magnetic transfer functions (VTFs). Remote reference data processing (Egbert 1997) is also used to improve the data quality at few noisy sites.

2.1 Dimensionality and directionality analysis

Geoelectric strike directions and dimensionality parameters such as skew values of the main profile were already discussed in detail in Meqbel *et al.* (2013). Here, we give a brief summary: Data from stations located at the eastern and western rift shoulders are consistent with approximately N–S striking regional 2-D structures, while data from stations within and close to the DSB are affected by 3-D features, such as the highly conductive Dead Sea brines. The geoelectrical strike directions were computed using the ellipticity criterion described by Becken & Burkhardt (2004). Fig. 2(a) shows strike direction estimates of the main and in-basin profile data, (b) pseudo-sections of skew values and phase tensor ellipses (Bahr 1988; Caldwell *et al.* 2004) for both, ((c) and (d)) the main and in-basin profiles. The rose diagrams of strike direction (Fig. 2a) at the western and eastern segments indicate a dominant N–S strike direction. Strike directions at central stations show greater variation but a predominant N–S direction can still be recognized. The rose diagrams also show the 90° ambiguity of the calculated strike direction. The phase-sensitive skew values (Bahr 1988) along the main profile show increased values (>0.3) for periods >8 s at stations located within the DSB (Fig. 2b). At some stations in the DSB high skew values are even observed at periods as short as 0.1 s. Generally low skew values at the western and eastern rift shoulders and high values in the DSB confirm the strike direction analysis: The impedances on the eastern and western rift shoulders are compatible with 2-D structures, whereas the central part is influenced by 3-D subsurface structures. Figs 2(c) and (d) summarize results of the phase tensor analysis for comparison. Phase tensor β -values exceed (> $\pm 3^\circ$) for periods >8 s at stations located along the main and in-basin profiles. The largest β -values (> $\pm 5^\circ$) are observed at stations located close or inside the DSB for periods >10 s. High $|\beta|$ values are also observed at periods >10 s at stations of the in-basin profile (Fig. 2d). The relatively large $|\beta|$ values at periods >8 s indicate the presence of 2-D structures at great depths striking in ~N15°E direction. Clearly, the electromagnetic fields recorded at stations located within the DSB are affected by 3-D structures, which can be expected in view of the complex geological and tectonic setting of this area. Consequently, and contrary to the eastern and western rift shoulders, the geoelectric strike direction of the in-basin stations appears scattered and without a predominant regional strike direction.

The VTFs describe the relationship between the horizontal and vertical magnetic field components; they are sensitive to lateral conductivity contrasts. This complex-numbered quantity is usually presented as induction vectors (IV) in map view for all stations at a particular frequency. IVs vanish if the subsurface within the

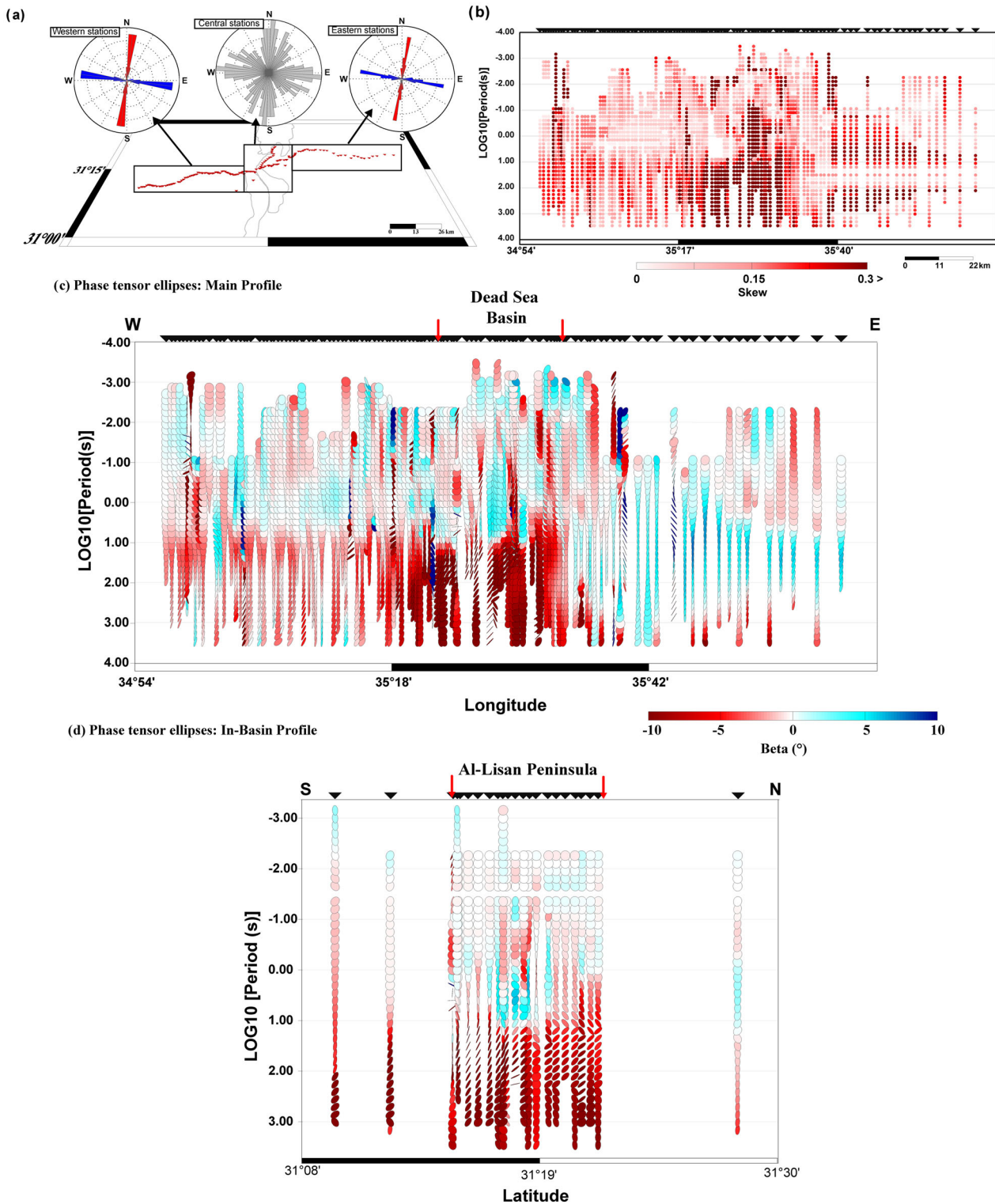


Figure 2. (a) Strike directions computed in the period range 1–1000 s for different segments of the main profile. (b) Phase-sensitive skew values along the main profile (Bahr 1988). (c) and (d) show pseudo-sections of phase tensor (Caldwell *et al.* 2004) data of stations located along the main and in-basin profiles, respectively. The colours of the ellipses indicate the size of the β -values (see the text).

induction volume (period dependent) is homogeneous or layered (Weaver 1994). In Wiese convention (Wiese 1962), the real parts of the IVs tend to point away from conductive areas where electrical currents are concentrated.

Fig. 3 shows the real parts of the IVs for four different periods. At almost all stations, the IVs at short periods (<1 s) are very small, indicating the absence of large and strong lateral conductivity contrasts. A few stations at the westernmost end of the profile show

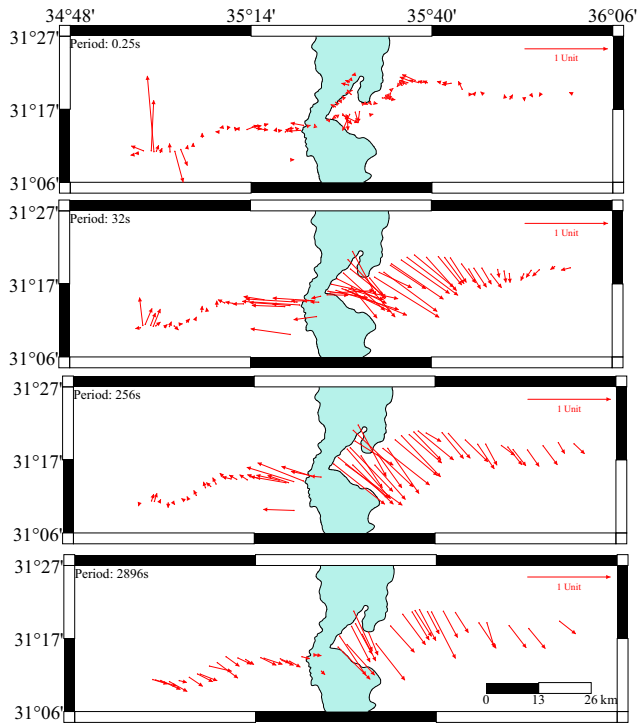


Figure 3. Real parts of the induction vectors (IV) presented in the Wiese convention (Wiese 1962) at four selected periods. The most pronounced feature, visible already at a period of 4 s, is a reversal of the IVs across the Dead Sea. But significantly large and south-eastwards pointing IV are observed at long periods at most stations. The general trend of the IVs is consistent with a regional strike in approximately predominantly north-south direction. For clarity, we plotted only the IVs of every second station.

longer vectors which may be due to very local geological features or electromagnetic noise. The IVs for longer periods at stations close to the western shore of the Dead Sea point mainly westwards, their lengths increase between 4 s up to 256 s and decrease again at periods >256 s. East of the Dead Sea and along the western coast of the Al-Lisan Peninsula, the direction of the IVs is approximately $N135^{\circ}E$ rather than perpendicular to the eastern shore of the Dead Sea. This indicates a more complex geometry of conductive features, while the east- or westward pointing IVs of stations of the central part of the study area are indicative for a conductor elongated in N-S direction, which could be explained by the high conductive Dead Sea brines and the underlying sediments. Additional conductivity features are indicated by IVs of the westernmost stations at the longest periods, which could be related with the Mediterranean Sea, which is located approximately 100 km west of the profile.

3 2-D INVERSION OF THE MT DATA

Prior to 2-D inversion, the impedance tensor data and the VTFs must be rotated into a coordinate system aligned with the geoelectric regional strike direction. Following the discussion above (see Figs 2 and 3), we chose a geoelectric strike direction of $N12^{\circ}E$. After rotation of the impedance tensor, the xy -component is in the E-polarization (TE-mode) with electric currents flowing parallel to the strike direction. Electric current flow perpendicular to the strike direction is assigned to the B-polarization (TM-mode). Fig. 4 shows the rotated data as pseudo-sections of apparent resistivity and phases. The most pronounced feature comprises very low ap-

parent resistivity values ($<1 \Omega m$) for all stations in the Dead Sea area (Fig. 4, label A). At longer periods (>10 s), we observe differences between the TE- and TM-mode apparent resistivity curves (Fig. 4, label B). The TM-mode apparent resistivities are by one order of magnitude more resistive than the TE mode and the TM-mode phases are at least 10° lower than the respective TE-mode. This difference between the modes at longer periods indicates at least 2-D regional structures at depth. Another interesting feature can be seen at stations located within the DSB at periods between 1 and 10 s. We note an increase in the apparent resistivities (Fig. 4, label C) and correspondingly low phases of 10° for the TM-mode and approximately 20° for the TE-mode. This spatially localized feature indicates a resistive structure embedded in a highly conductive host. Data of stations located to the east and west of the Dead Sea and for periods <10 s are consistent with a 1-D nature of the shallow subsurface (Fig. 4, label D).

For 2-D inversion, we used the regularized non-linear conjugate gradient (NLCG) algorithm described by Rodi & Mackie (2001). This algorithm is implemented in the WinGLink software package. The model mesh used for the 2-D inversion consists of 248×127 cells in y - and z -directions. Cell widths are almost linear in the area of interest with an average value of approximately 300 m and increase logarithmically outwards to avoid any influence from model boundaries. The cell thicknesses, particularly for the upper 5 km of the model, were chosen thin enough to ensure accurate solution of the differential equations for the high-frequency data. As fine vertical gridding is also required to recover shallow structures we set a thickness of 20 m for the first layer, thicknesses of all subsequent layers increase logarithmically by a factor of 1.1. We also included topography and a rough bathymetry of the Mediterranean Sea as *a priori* information for the inversion. The entire model domain extends from $-10\,000$ to $10\,000$ km in horizontal directions and to a depth of 3500 km in the vertical direction.

We ran numerous inversions to test the influence of a wide range of inversion parameters, such as assessing the influence of individual data types (TE, TM and VTFs), model discretization and regularization parameter. Fitting the TM-mode and VTF data separately results in similar models, while inversion of the TE-mode (apparent resistivity and phase) shows different structures in the vicinity of the DSB. If only the TE-mode phases are fitted, the inversion model is consistent with the results of inversions of TM-mode and VTFs. As the apparent resistivity data of the TE-mode at stations close the DSB are strongly affected by 3-D inhomogeneities and/or by static shift, they were excluded from the 2-D inversion.

For the preferred 2-D inversion model in Fig. 5, we used all available data components (TE-, TM-modes and VTF's; excluding TE-mode apparent resistivity) and the full period range from 0.001 to 3000 s. A 5 per cent error floor was set for the TM-mode apparent resistivities and 0.6° to the TM- and TE-mode phases. A constant error floor of 0.03 was set to the vertical magnetic components. Apart from topography and bathymetry of the Mediterranean Sea ($0.3 \Omega m$), a homogeneous background of $100 \Omega m$ was used as starting model for the 2-D inversion.

For the model in Fig. 5(a), approximately 2000 NLCG iterations were required to reduce the overall normalized root mean square value (nRMS) from 12.5 to 1.8 (computed for all sites, all data points and all periods) which is acceptable for the assigned error bounds. The nRMS values for individual stations (see Fig. 5b) indicate that sites located at the eastern and western rift shoulders are generally well fitted. Relatively high nRMS values for the central stations are indication for an influence of 3-D features, which cannot be modelled with 2-D inversion.

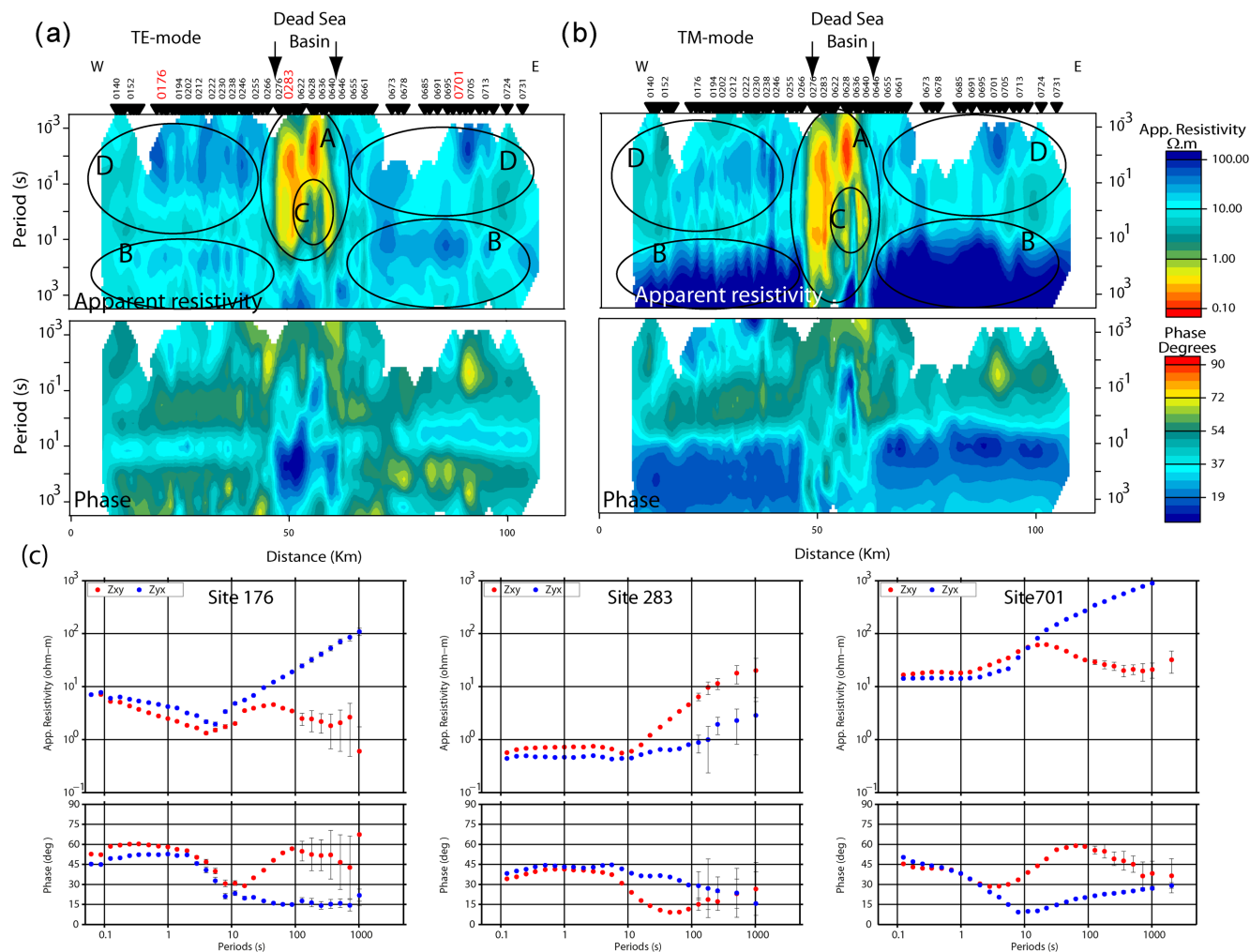


Figure 4. Pseudo-sections of apparent resistivity (upper panels) and phases (lower panels) for (a) TE-mode and (b) TM-mode along the main profile. Low apparent resistivity values ($<1 \Omega m$) are observed at stations located in the Dead Sea Basin. Letters A, B, C and D denote areas with similar apparent resistivity and phase characteristics for the TE- and TM-modes (see the text for further explanation). (c) Apparent resistivity and phase curves of three selected sites (labelled in red in (a)) from the western and eastern rift shoulders (sites 176 and 701) and the Dead Sea Basin (site 283). Most prominent is a drop in the general levels of the apparent resistivities curves to values below $1 \Omega m$ for stations located in the Dead Sea Basin.

Several interesting features, labelled as A, B, C, D, D1, E and F, can be identified in Fig. 5(a). Two resistive blocks A and B ($>1000 \Omega m$) extend from approximately 2.5 km to several tenths of kilometres depth. On top of these two resistive blocks (A and B) appear sequences of alternating conductive and moderately resistive layered material (labels C and E). Highly conductive structures D ($<5 \Omega m$) are observed directly beneath the DSB to a depth of approximately 5 km. The high conductivity appears to be interrupted by moderately resistive material at shallow crustal levels (D1). All of the structures revealed in the upper 5 km of the crust (labels A, B, C, D, D1 and E) were discussed in detail in Meqbel *et al.* (2013). For this study we focus on the implications for the deeper crust and upper mantle, particularly on feature F in Fig. 5(a).

This deep-reaching, subvertical conductive region labelled F is a very pronounced and dominant feature of the 2-D inversion models, which separates the two resistive blocks of the eastern and western rift shoulders at depths >10 km. The resistivity of F varies between 1 and $10 \Omega m$, with the lowest values being observed at depths between 30 and 40 km. Horizontally, conductor F extends for approximately 25 km (between profile km 30 and 55), and vertically, to a depth of approximately 60 km. At shallower depths, the conductor is inclined

to the east and seems to be connected to the shallow basin conductor (labelled D) at a depth of approximately 10 km.

Judging from the nRMS values computed at each site (Fig. 5b), our preferred model fits the data within the assigned error bounds. To further test if the deep subvertical conductor is a required feature, we use constrained inversions. We adopted the so-called ‘fix and invert’ approach, for which particular structures of the conductivity model are kept fixed, the inversion is re-run and eventually the resulting new data misfits are analysed. Following this approach, we replaced all structures from the deeper part of the inversion model with resistivities of $1000 \Omega m$ and locked all cells below depths of approximately 18 and 30 km. Resistive blocks A and B were also set to resistivity values of $1000 \Omega m$. For the constrained inversions, we used the same data types, error setting, model discretization and inversion parameters as for the preferred model (Fig. 5).

Figs 6(a) and (b) show the constrained inversion results together with the corresponding nRMS values for each site. The inversion with fixed model parameters below a depth of 18 km stopped with an overall nRMS of 5.8. If the inversion cannot alter any of the structures below 18 km depth, this results in a significantly worse data fit (*cf.* Fig. 6c) at almost all sites when compared to the preferred

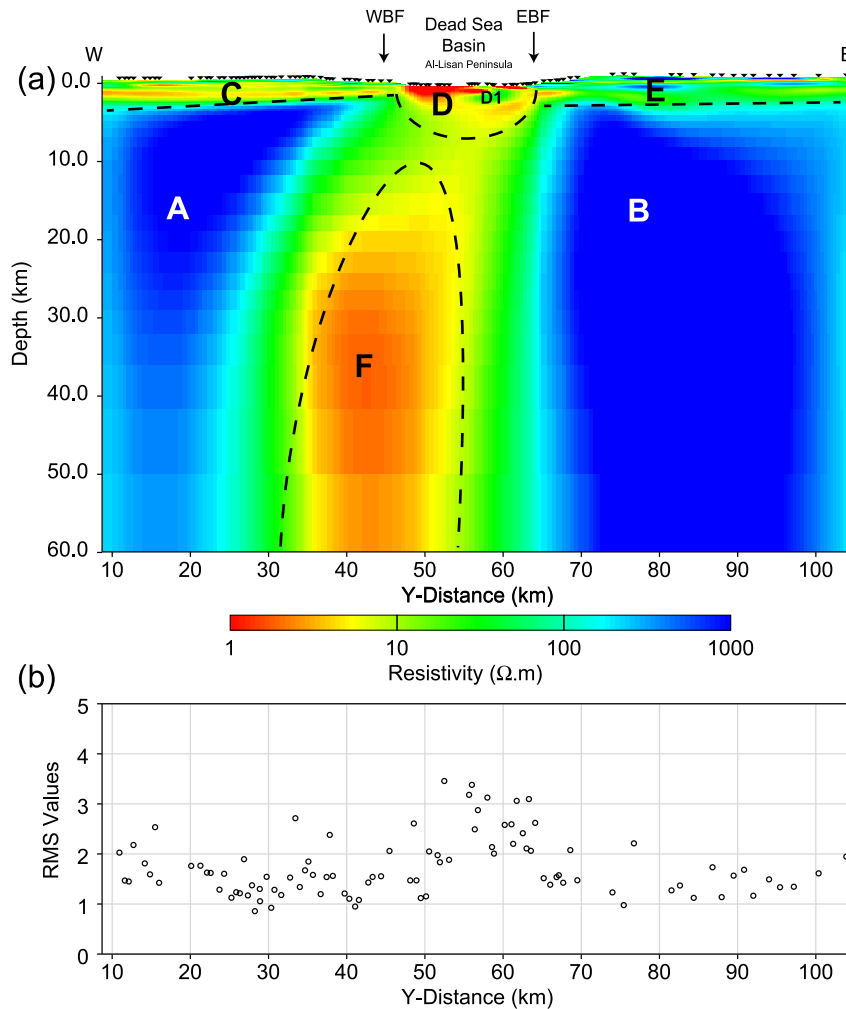


Figure 5. (a) The preferred 2-D electrical resistivity model. Red and yellow colours mark zones of low resistivity. Labels A–F mark distinct but robust features which are discussed in more detail the text. The most prominent feature is a subvertical zone of low resistivity (label F) which extends to a depth of ~ 80 km. (b) Computed normalized RMS values (nRMS) at each station along the profile (see the text).

model in Fig. 5. To compensate for the absence of the deep subvertical conductor F, the constrained inversion attempts to include cells with even higher conductivity (up to $0.1 \Omega\text{ m}$) at depth and we observe a widening of the conductive material towards shallower levels (Fig. 6a). Interestingly, all other structures of the upper 5 km remain roughly the same. Similarly, fixing model parameters below a depth of 30 km results in an accumulation of conductive ($\leq 1 \Omega\text{ m}$) structures towards the top of the constrained zone (Fig. 6b). Improved data fits are observed (Fig. 6d) in comparison to the model in (Fig. 6a) where resistivities were fixed below 18 km. However, worse data fits are observed at sites located at the eastern rift shoulder when compared to the data fits of the unconstrained (preferred) inversion results (green dots in Fig. 6d). We conclude that in order to fit the MT data, particularly at long periods, highly conductive material is required for the region beneath the DSB, which must extend to at least lower crustal depths.

4 DISCUSSION OF THE 2-D ELECTRICAL CONDUCTIVITY MODEL

Fault zone conductors (FZC) in the mid- and lower-crust caused by shear movements along major strike-slips faults have been observed worldwide using the MT technique (e.g. Ritter *et al.* 2003, 2005;

Unsworth & Bedrosian 2004; Tank *et al.* 2005; Thiel *et al.* 2009; Becken *et al.* 2011; Desissa *et al.* 2013). The geometry and the overall conductance of FZCs depend on local geological, hydrogeological conditions and the geodynamic (tectonic) setting of a fault (see Unsworth & Bedrosian 2004; Ritter *et al.* 2005, and references therein).

Ritter *et al.* (2003) interpreted MT data collected along a profile across the Araba fault (a segment of the DST) which is located ~ 150 km to the south of the DSB. The 2-D conductivity model for the upper 5 km of the crust suggested that the Araba fault acts as an impermeable barrier to cross-fault fluid transport and also that the damage zone of the DST is exceptionally narrow (metres range wide). A 3–5 km wide, subvertical FZC is imaged in the crust and upper-mantle west of the Araba Fault, which is spatially confined even in the ductile lower crust, but the bottom of the conductor is not resolved (Weber *et al.* 2009).

At the DSB, and contrary to the Araba Fault, the DST has a very significant extensional component which causes splitting of the DST into two fault strands and the formation of a very large pull-apart basin (Garfunkel *et al.* 1981; Garfunkel 1981). Petrunin & Sobolev (2008) concluded from thermomechanic modelling studies that such a deep and relatively narrow pull-apart basin could only form in initially cold lithosphere if the major faults had low

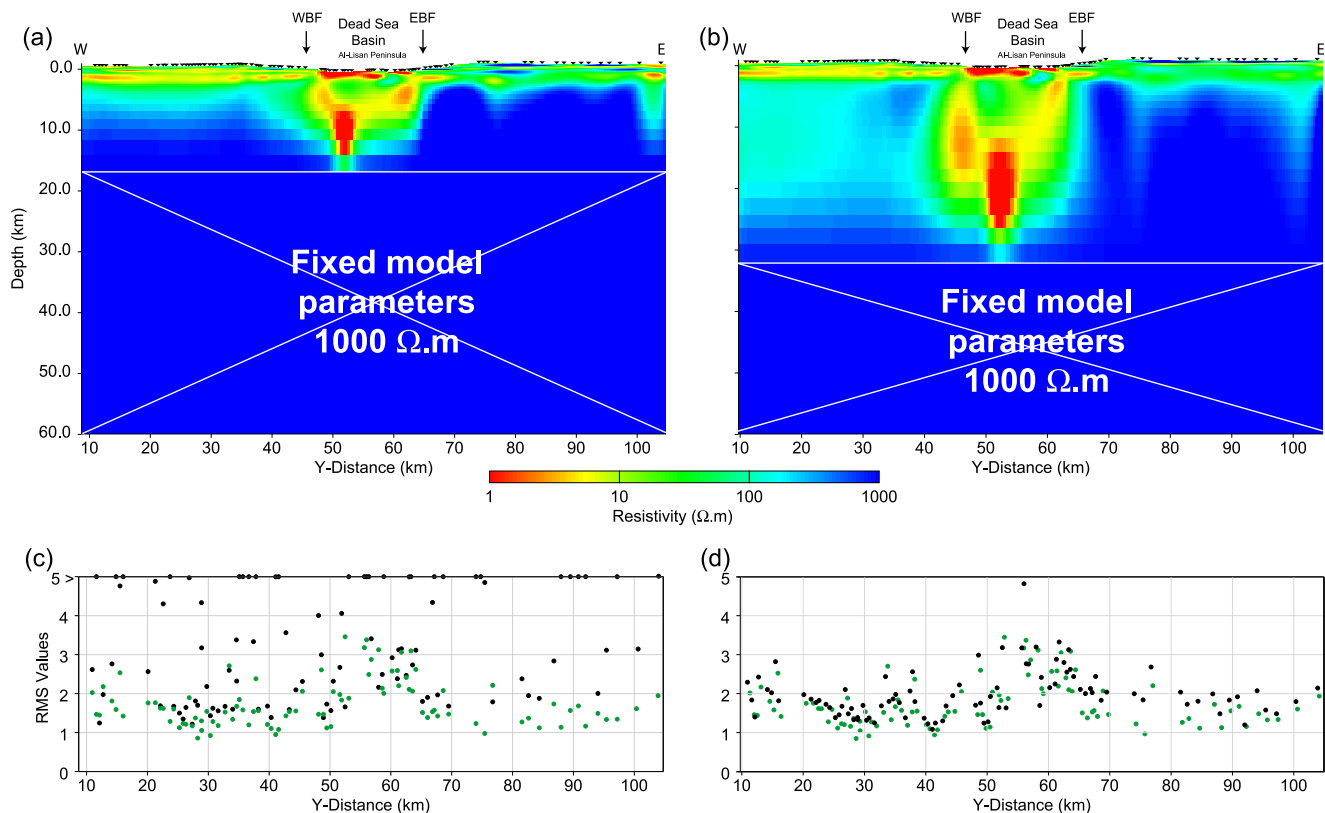


Figure 6. (a) and (b) 2-D resistivity models obtained by constrained inversions. The lower part (below ~ 18 and ~ 30 km) of the inversion model in Fig. 5 was set to $1000 \Omega \text{ m}$ and kept fixed for subsequent inversion runs. Black markers in (c) and (d) represent the normalized RMS values (nRMS) at each site. For comparison, the nRMS values for each site of the unconstrained inversion are plotted in green colour.

friction parameters of 0.1–0.2. Low friction conditions imply the presence of hydrous minerals and/or fluids. Alteration of granitic rocks which include Feldspar to varieties of hydrous minerals including Muscovite have been observed at deeper levels in many fault zones (Etheridge *et al.* 1983; Bruhn *et al.* 1990). Based on thermomechanic modelling, Petrunin *et al.* (2012) suggested that the state of the DSB as a classical pull-apart basin can be explained by thermal erosion of the lithosphere before approximately 20 Myr. As a consequence, we would expect relatively weak rheology of the uppermost mantle which would be consistent with the occurrence of wet olivine or pyroxenite (Petrunin *et al.* 2012).

The deep subvertical conductive region F in Fig. 5 is likely linked to shear deformation of the DST in the middle and lower crust and related processes. High conductivities in active tectonic zones have often been associated with fluids and hydrous minerals (Boerner *et al.* 1998; Unsworth & Bedrosian 2004; Jones *et al.* 2005; Ritter *et al.* 2005; Wannamaker 2005; Becken *et al.* 2011; Meqbel *et al.* 2014). For instance, Becken *et al.* (2011) interpreted a subvertical conductive anomaly extending through the entire crust north-west of Parkfield in California as a migration path for deep (partly mantle derived) fluids into the San Andreas Fault system. Signatures of mantle derived fluids in surface waters have been reported from major strike-slip faults around the world (e.g. Kennedy *et al.* 1997). For the DST system, Friedman *et al.* (1999) suggested from analysing strontium isotopes that mantle-derived fluids contributed to the formation of dolomites found close to hot springs along the eastern side of Dead Sea rift valley. Eraifej (2006) measured high $^3\text{He}/^4\text{He}$ ratios of samples collected from wells and springs along the DST and close to the eastern part of the DSB. Anomalously

high $^3\text{He}/^4\text{He}$ in geothermal fluids indicate that these geothermal systems are associated with more rapid upwelling of mantle derived fluids (Siler & Kennedy 2016). More recently, Schaeffer & Sass (2014) investigated thermal water samples from the eastern side of the Dead Sea valley and suggested that the high geothermal gradient could be best explained if water of deep origin invaded the hydrothermal system of the DSB. Sources of fluids for this particular tectonic setting at middle to lower crustal levels could in general include: (i) fluid influx from the surrounding Precambrian crust due to large negative vertical stress beneath the less dense sedimentary basin material (Ten Brink & Flores 2012), (ii) dehydration of upper-mantle material within the shear zone, (iii) low- to high-grade metamorphic processes (Etheridge *et al.* 1983; Bruhn *et al.* 1990), (iv) generation of hydrous minerals by retrograde metamorphism (Etheridge *et al.* 1983) and (v) some combination of these processes. Fig. 7 shows a conceptual model summarizing these ideas.

Ruling out a major contribution from shear heating, a hypothesis that seems plausible for low friction coefficients and slip rates (Leloup *et al.* 1999), the observed surface heat flow of $45\text{--}53 \text{ mW m}^{-2}$ would suggest temperatures between $280^\circ\text{C}\text{--}343^\circ\text{C}$ for a depth of 20 km and $387^\circ\text{C}\text{--}483^\circ\text{C}$ for a depth of 30 km (Al-Zoubi & ten Brink 2002, and references therein). Hence, middle- to low-grade metamorphism can be expected to occur at depths of approximately 30 km and retrograde metamorphism at depths of approximately 20 km (Etheridge *et al.* 1983). The formation of hydrous minerals in the lower crust leads to a release of water which has a tendency to migrate upwards. With decreasing temperatures, at depths of approximately 20 km, upwards-migrating fluids can

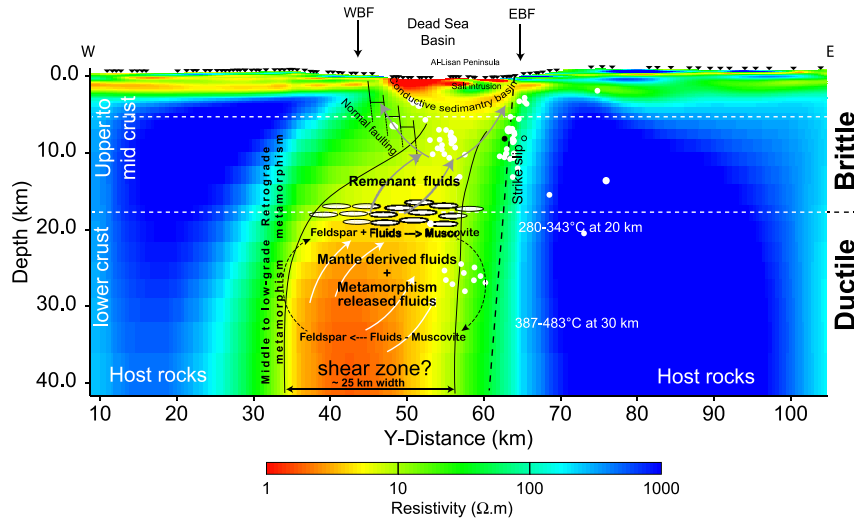


Figure 7. Conceptual model derived from integrating petrophysical, geological, hydrological, tectonic and geodynamic information with the preferred 2-D conductivity model. The subvertical conductive anomaly in the middle and lower crust underneath the DSB is interpreted as a 20–25 km wide system of shear zones, filled with fluids released from a range of sources. Fluids from the uppermost mantle mix with fluids released from middle to lower grade metamorphism (white arrows). Retrograde metamorphism at the brittle-ductile transition zone consumes some of these fluids by forming hydrous minerals such as Muscovite. Excess fluids migrate upwards (grey arrows) and mix with meteoric (surface) water. White dots show the positions of major earthquakes projected onto the section (after Braeuer *et al.* 2012). Horizontal dashed lines (white) indicate transition from upper to middle and lower crust after seismic velocity models (e.g. Aldersons *et al.* 2003; Mechie *et al.* 2009). WBF and EBF are, the Western and Eastern Boundary Faults, respectively.

be consumed by retrograde metamorphism, which causes Feldspar-rich rocks, such as granites, to be converted to rocks which are rich in hydrous minerals, such as Muscovite. Bruhn *et al.* (1990) argued that the strength of a Muscovite-rich rocks is substantially lower than the strengths for wet and dry granite or quartz. Muscovite-rich rocks form over time, a semi-permeable layer for fluids at mid-crustal levels (see Ten Brink & Flores 2012; Etheridge *et al.* 1983, and references therein). Fluids which are not consumed by retrograde metamorphism reactions continue to rise and eventually mix with ground water systems at surface. Ten Brink & Flores (2012) also proposed such a Muscovite-rich layer in the middle crust beneath the DSB to explain rapid subsidence rates. The conductivity distribution of our 2-D inversion model for the DSB supports such a scenario.

5 3-D INVERSION AND MODELLING

Geoelectric strike and dimensionality analysis (see Fig. 2) suggest an influence of 3-D structures, in particular at stations located in the central part of the study area (Dead Sea area). Obvious off-profile 3-D features are the highly conductive Dead Sea brines and the underlying sediments with variable thickness. To account for some of these effects, that is, to achieve some areal site coverage, we collected additional MT data along a much shorter in-basin profile (Fig. 1b).

For 3-D inversion, we used the Modular System (ModEM) of Egbert & Kelbert (2012) and Kelbert *et al.* (2014) with additions for parallel computing described by Meqbel (2009). ModEM is based on a finite-difference (FD) approach to solve Maxwell's equations on a staggered grid. Solving the EM forward modelling problem in 3-D requires placing the boundaries of the model domain far enough away from any inhomogeneities (e.g. Weaver 1994). Usually, a number of padding cells are attached to all sides of the model to ensure this condition is fulfilled. This results, however, in significantly increased grid sizes for model and inversion domains. To

overcome this problem, we adopted the so-called 'nested modelling' approach, in which the induction equations are initially solved for a coarser grid of a large regional-scale model. The coarse model includes realistic rough bathymetry of the Mediterranean and the Dead Sea. The electric field solution of the large model provides the boundary values (tangential electric field components) for a much smaller modelling domain, centred on the area of interest. This strategy considerably reduces size of the models and allows using a more uniform numerical grid, which in turn leads to overall faster convergence rates and improved accuracy of the forward modelling and gradient computations.

For the regional electric field solution, used subsequently for all nested modelling and inversions, we used a large grid, consisting of 70×70 cells in x - and y -directions, with a horizontal cell size of 2 km^2 in the central part and increasingly larger cell sizes towards the edges of the model. For gridding the vertical (z -) direction, we had to consider fairly steep topography (from 1300 m a.s.l to 420 m b.s.l), a wide frequency range of the observations and very low apparent resistivities of the Dead Sea brines. Eventually, we used 37 layers with thicknesses of 50 m each, followed by 53 layers with logarithmically increasing thicknesses (factor of 1.1). This results in a total number of 90 layers in the vertical direction and a lower model boundary of 425 km. We also added ten air layers. All 3-D inversions were started and penalized against a homogeneous half-space of $100 \text{ } \Omega \text{ m}$ which had the Dead Sea brines ($0.2 \text{ } \Omega \text{ m}$) and the Mediterranean Sea ($0.3 \text{ } \Omega \text{ m}$) included as *a priori* information.

For the 3-D inversions, we used the full impedance tensor (\mathbf{Z}) and the vertical magnetic field components (\mathbf{Tz}) from a subset of stations from both the main and in-basin profiles, using 20 periods in the range between 0.01 and 2000 s. We assigned error floors of 5 per cent of $\sqrt{|Z_{xy}Z_{yx}|}$ to the four complex impedance tensor components. A constant value of 0.03 was used as an error floor for the vertical magnetic field components. Contrary to the 2-D inversion, the data were not rotated for 3-D inversion. Some heavily biased or scattered data points were discarded by visual inspection.

Handling the regularization parameters in NLCG algorithms is very important. In ModEM, rapid or continuous changes of the regularization parameter λ (lambda) during the inversion process can result in a loss of orthogonality of the search direction vectors in the NLCG algorithm. On the other hand, using a fixed value of λ can cause the NLCG algorithm to get stuck in local minima. For the 3-D inversion results presented in this study we used the following procedure to update λ : (i) the inversion is started with a value of 1.0; (ii) at each iteration, the difference between the data misfit (in terms of RMS) of the current and previous iterations is computed and (iii) if the differences between the RMS values is below a certain threshold (e.g. <0.002) we decrease the value of λ by dividing its current value by a factor of 10. The value of λ is decreased in the third step to ensure the NLCG algorithm can escape from a local minimum. We choose a very small threshold value (<0.002) to avoid a rapid change of λ to ensure that orthogonality of the search direction vectors is maintained.

Determining appropriate smoothing parameters in ModEM is crucial as they depend on many factors including cell sizes. For the results presented in this study, we tested a range of smoothing parameters to ensure good data fit but keeping structures connected. The smoothing parameters were kept fixed during all inversion runs discussed in this study.

Appropriate gridding is essential to find a good compromise between model dimensions (computation time), accuracy of the numerical solutions and optimum data fit. Fig. 8 shows an example of two nested modelling inversion runs using the full data set ($\mathbf{Z}+\mathbf{Tz}$) and two different model discretizations. First, a coarse nested grid was constructed using horizontal cell sizes of 2 km^2 and a minimum cell thickness of 50 m (similar to the outer larger grid). For the finer, nested model grid, we subdivided all horizontal cells in the vicinity of site locations and the vertical cell thicknesses to a depth of 100 km by a factor of 2. The coarse grid comprised of $30 \times 54 \times 69$ cells in the x -, y - and z -directions, while the finer grid contained $49 \times 108 \times 90$ cells. The core modelling area of the coarse and fine grids is 60 km in NS (or x -) direction and 112 km in EW (or y -) direction. This core area is nested into a larger modelling domain with dimensions of 322×322 km. Comparison between the two inversion results in Fig. 8 reveals significant differences. The much smaller data misfits and consistency of the obtained structures all suggest that the finer nested grid is required.

The topography along the main profile varies between ~ 1300 m above sea level at the eastern rift shoulder and ~ 430 m b.s.l at the Al-Lisan Peninsula. The FD code used for this study (ModEM) does not account for horizontal conductivity contrasts (i.e. between earth and air) when interpolating the EM fields at surface. It is therefore not straightforward to include topography in a 3-D model. To increase numerical stability, it is essential to ensure that there is at least one horizontal cell between a cell which contains a site and an air cell.

Fig. 9(b) shows a comparison between inversions with and without topography along the main profile. The strongest topography gradient is near the DSB and Fig. 9(c) shows that only the inverse model with topography resolves the expected stacks of sub-horizontal layers on both rift shoulders, that is, consistent with structures labelled C and E in the 2-D inversion (Fig. 5). Layered sedimentary sequences are also consistent with geological and hydrological information (see Meqbel *et al.* 2013, and references therein). The inverse model without topography, on the other hand shows one (integrated) thick conductive layer at each side. Comparison between the data fits of the two inversion runs (Fig. 9d) indicates, however, that the impedance data (\mathbf{Z}) is slightly better fit-

ted by the inversion without topography; the reasons are not entirely clear.

It is well known that impedance tensor and vertical magnetic field data have different resolution capabilities with respect to horizontal and vertical subsurface conductivity contrasts (e.g. Vozoff 1991). To better understand which structures are required by a particular data component, we also show 3-D inversion results for \mathbf{Z} and \mathbf{Tz} separately. The middle and right columns of Fig. 10(a) show the same depth slices as in Fig. 8, the left column shows results of a joint inversion (\mathbf{Z} and \mathbf{Tz}) for comparison.

When fitting the impedance data we observe a stripe of conductive structures at shallow depths ($\lesssim 5$ km) which follows the main profile trace, and which is absent in the \mathbf{Tz} model. On the other hand, a very pronounced (and expected) lateral conductivity contrast between resistive and conductive structures associated with the DSB (underneath the Al-Lisan Peninsula) is almost exclusively observed when fitting the \mathbf{Tz} data. At depths $\gtrsim 5$ km, the impedance tensor only inversion reveals resistive material beneath the main profile, consistent with the expected Precambrian basement rocks. In contrast, the inversion model fitting \mathbf{Tz} indicates two other lateral conductivity contrasts, with zones of high conductivity to the southwest of the Al-Lisan Peninsula and to the north of the eastern Rift shoulder. The joint inversion result in the left column of Fig. 10 is clearly dominated by structures required to fit the impedance data, as most of the structures revealed by the vertical magnetic field only inversion are not recovered. Consequently, the \mathbf{Tz} data show much larger misfits in comparison to the \mathbf{Tz} -only inversion (Fig. 10b).

To find a better balance between the two data sets for a joint inversion, we developed a so-called 'Combined inversion approach' in which the inversion is started with a model containing *a priori* structures and not just a homogeneous background model. We further examine two strategies: (i) using the \mathbf{Tz} -only inversion result (Fig. 11, middle column) as starting model and (ii) taking the average model of the two individual inversions as starting model (Fig. 11, right column). As before, all inversions are penalized against the same prior model, which consists of a homogeneous half space ($100\ \Omega\text{ m}$) and the Dead Sea brines ($0.2\ \Omega\text{ m}$).

Fig. 11 shows a comparison of these different inversion strategies. Structures of the upper ~ 5 km beneath the eastern and western rift shoulders are largely similar. Discrepancies occur towards the central part at depths > 5 km. When starting the inversion from a model fitting \mathbf{Tz} data (middle column in Fig. 11b), the strong lateral conductivity contrasts required by \mathbf{Tz} data are maintained. Particularly, the resistive structures underneath the Al-Lisan Peninsula are kept. At depths > 10 km, the eastern rift shoulder is imaged with resistivities $> 500\ \Omega\text{ m}$, much higher when compared to the inversion which started from a $100\ \Omega\text{ m}$ half-space (left column). In the region of the DSB, we observe a pronounced subvertical, westward dipping structure in a depth range of 10–25 km. These deeper features are also visible when starting the inversion from the averaged (\mathbf{Tz} , \mathbf{Z}) model (right column), but not for the 'standard' joint inversion approach which results in a model with hardly any structures at depth (left column).

Fig. 11(c) shows a similar comparison along the north–south trending in-basin profile. The most pronounced feature, revealed by all three inversions approaches, is a southward dipping conductor extending from shallow depths close to the Al-Lisan Peninsula to depths of approximately 10 km. Structures underneath the Al-Lisan Peninsula, however, appear differently. If the \mathbf{Tz} data contribute to the inversion (middle and right columns in Fig. 11c), the high resistive material beneath the Al-Lisan Peninsula splits into two parts: a smaller, shallower northern section and a larger, thicker

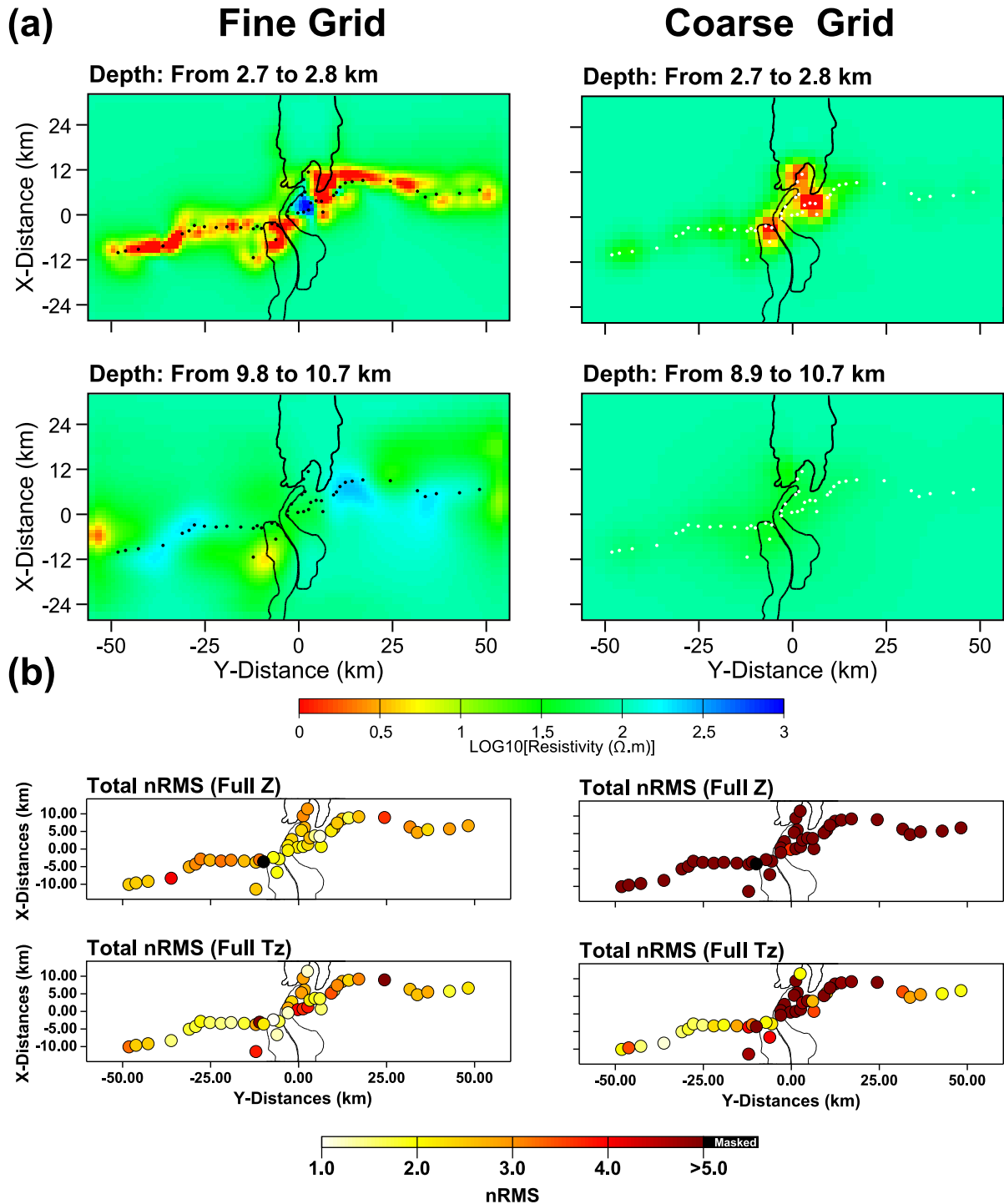


Figure 8. (a) Two depth slices from the 3-D inversion results obtained using fine (left column) and coarse (right column) grids. (b) Data fits are presented as nRMS at each site for the full impedance tensor (Z) and the vertical magnetic transfer functions (T_z). The coarse grid results in sparse and incoherent structures and significantly worse data fit.

southern part. Further differences between standard and combined inversion approaches become evident when looking at the ~ 12 km depth slice in the map view (Fig. 11d). Particularly, a conductive region north of the eastern rift shoulder is only evident for the combined inversion approach (middle and right columns).

To assess the quality of the three inversion models, Fig. 11(e) shows nRMS values (averaged over all periods at each site) for the off-diagonal elements of the impedances and the VTFs. Overall, the

achieved nRMS values are acceptable. When using the combined inversion approach the nRMS values decreased from an initial value of ~ 8 to 2.3 after 84 NLCG iterations. The conventional inversion approach required 120 NLCG iterations to reduce the nRMS from an initial value of ~ 63 to 2.7. Another general observation for all three inversions is a worse fit of the Z_{yx} component when compared with the other impedance components. The fit of the vertical magnetic fields is worse for the combined inversion approaches when

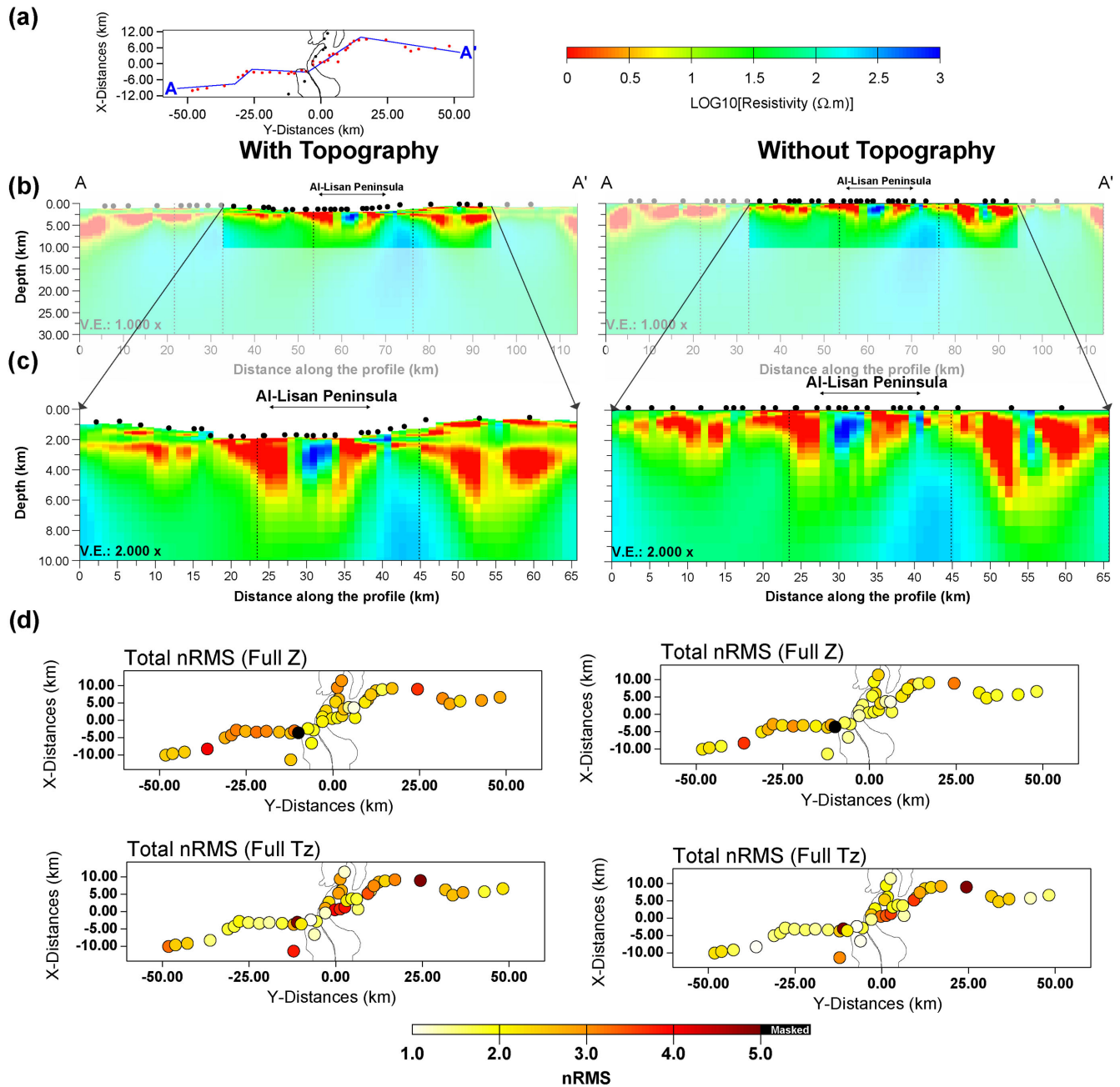


Figure 9. A comparison between 3-D inversion results with and without topography. (a) Location map showing the transect (A–A′). Red dots in (a) indicate sites projected onto section A–A′. (b) and (c) show cross-sections through the 3-D inversion models following the transect. (d) Data fit presented as nRMS at each site for the full impedance tensor (**Z**) and the vertical magnetic transfer functions (**T_z**). Inclusion of topography for the 3-D inversion reveals layered structures in the uppermost crust which are more consistent with the 2-D inversion functions model in Fig. 7 and with geological information.

compared with **T_z**-only inversion (Fig. 10b, middle column) but significantly better, particularly for the **T_{zy}**, components of sites located towards the north and east, when compared to the conventional joint inversion (left columns of Fig. 11b). Overall, the best compromise may be obtained by starting the inversion from the averaged model.

6 INTERPRETATION OF THE 3-D MODEL

Fig. 12 shows our preferred 3-D model in map view at eight selected depths from the uppermost crust to mid-crustal levels. It also shows

cross-sections along the main and in-basin profiles. To simplify comparison with the 2-D inversion model in Fig. 5, we use similar labels to describe features of the 3-D model. Contrary to the 2-D model, we refer to depths in the 3-D model relative to the highest point of the topography, which is approximately 1300 m a.s.l. For the top ~1 km, the 3-D model reveals conductive structures (sedimentary sequences) along the eastern and western rift shoulders (labelled E1 and C1). Similar to the 2-D model (Fig. 5), we observe higher resistivity between 1 and ~1.6 km beneath the eastern and western rift shoulders (Figs 12a and b) and extremely conductive structures associated with the Dead Sea brines (label D; Fig. 12c). At depths between ~1.6 and ~3 km, conductive structures E2 and

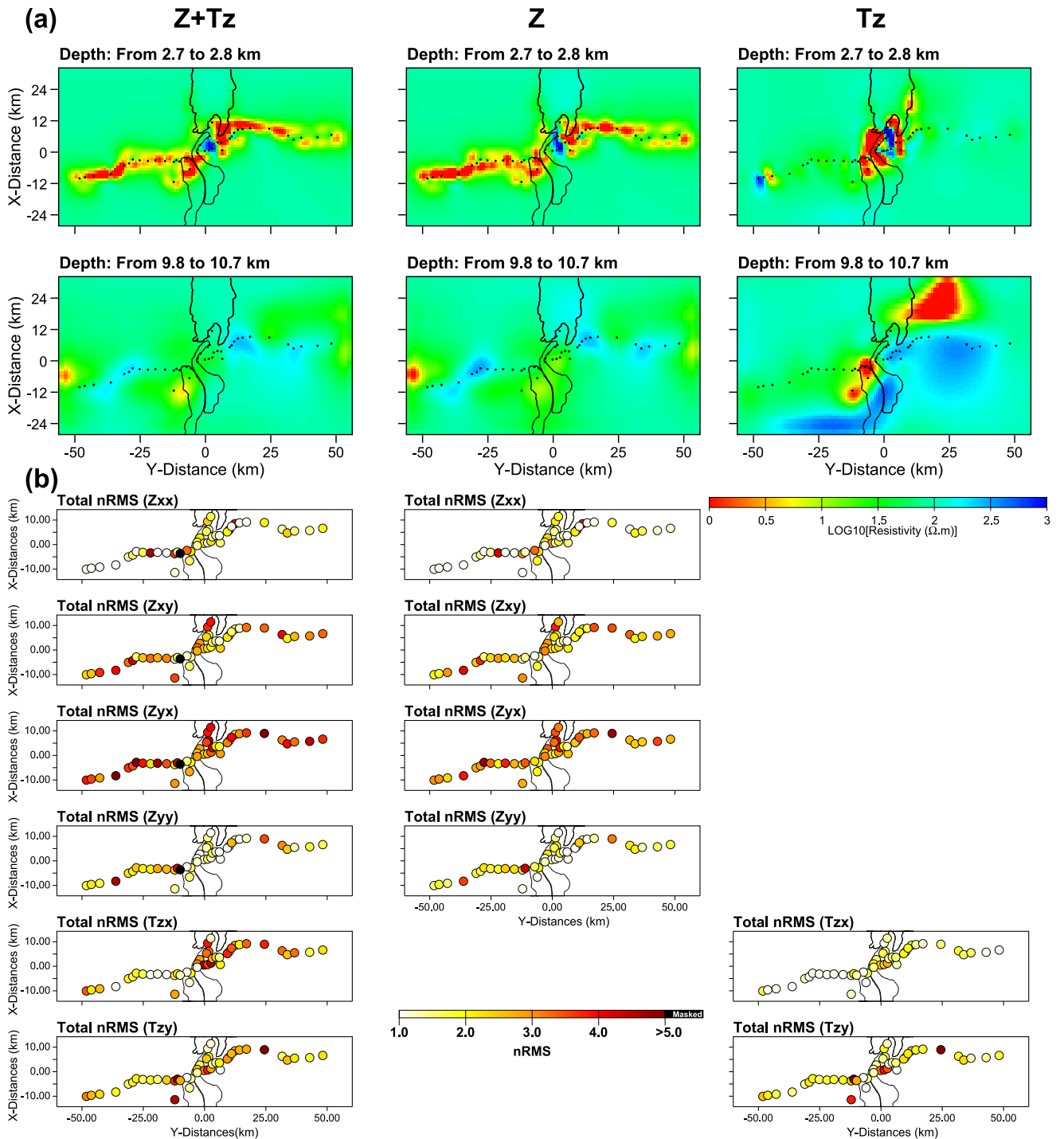


Figure 10. (a) Comparison between 3-D models inverted for **Z** and **Tz** jointly (left column) and separately (middle and right columns). The results are presented at two depth slices. (b) shows the corresponding data misfits (nRMS values) at each site. The joint inversion (**Z** and **Tz**) results in a model dominated by structures required to fit the impedance data, and consequently a worse data fit for the vertical magnetic field data (see the text).

C2 (Fig. 12d) are imaged along the main profile beneath the eastern and western rift shoulders. The area of the Al-Lisan Peninsula is associated with a spatially confined resistive structure (D1).

The sequences of conductive (E1, E2, C1 and C2) and resistive layers observed along the main profile are consistent with the 2-D inversion results (Fig. 5). We interpret these structures as systems of aquifers extending along the eastern and western rift shoulders

(Meqbel *et al.* 2013). The spatial correlation of the resistive body D1 with the Al-Lisan Peninsula appears clearly in the 3-D inversion images (see Figs 13b and c). We interpret D1 as resistive rock salt, coincident with a massive crystallized Halite intrusion (the Al-Lisan salt diapir). The Al-Lisan salt diapir covers most of the Al-Lisan Peninsula and extends vertically to a depth of ~ 6 km (Figs 13b and c). This observation is consistent with seismic velocity models (e.g.

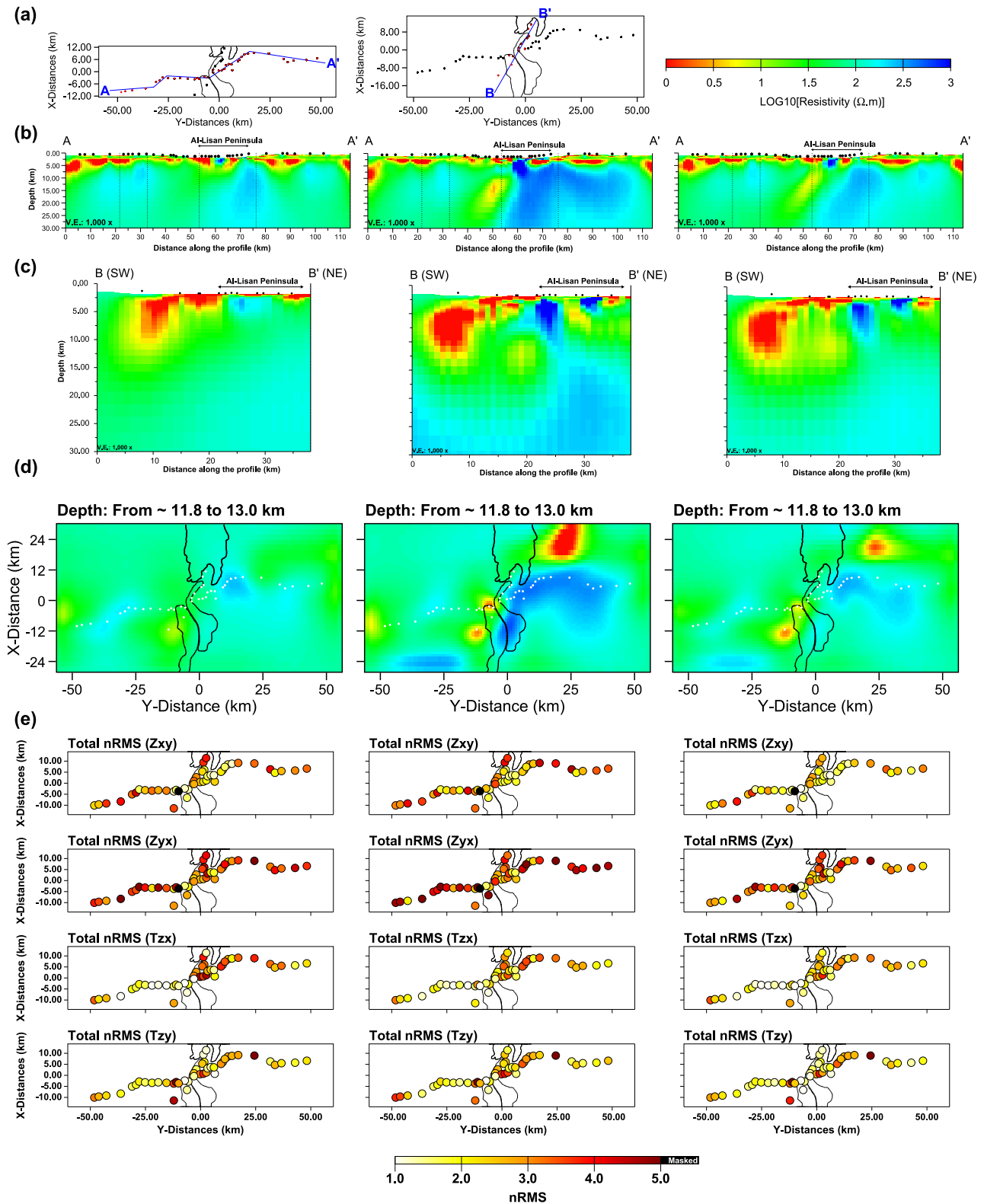


Figure 11. Comparison between 3-D inversion results using different starting models. (a) Location map shows the transects used to extract the cross-sections presented in (b) and (c). (d) shows a corresponding depth slice in map view. Left column (in (b)–(e)) shows inversion results when starting the inversion from a homogeneous half-space of $100 \Omega \text{ m}$. Middle column: inversion result obtained when starting from the model in Fig. 10 (right column). Right column: inversion result when using an average of the two individual inversions (fitting Z or T_z) as starting model.

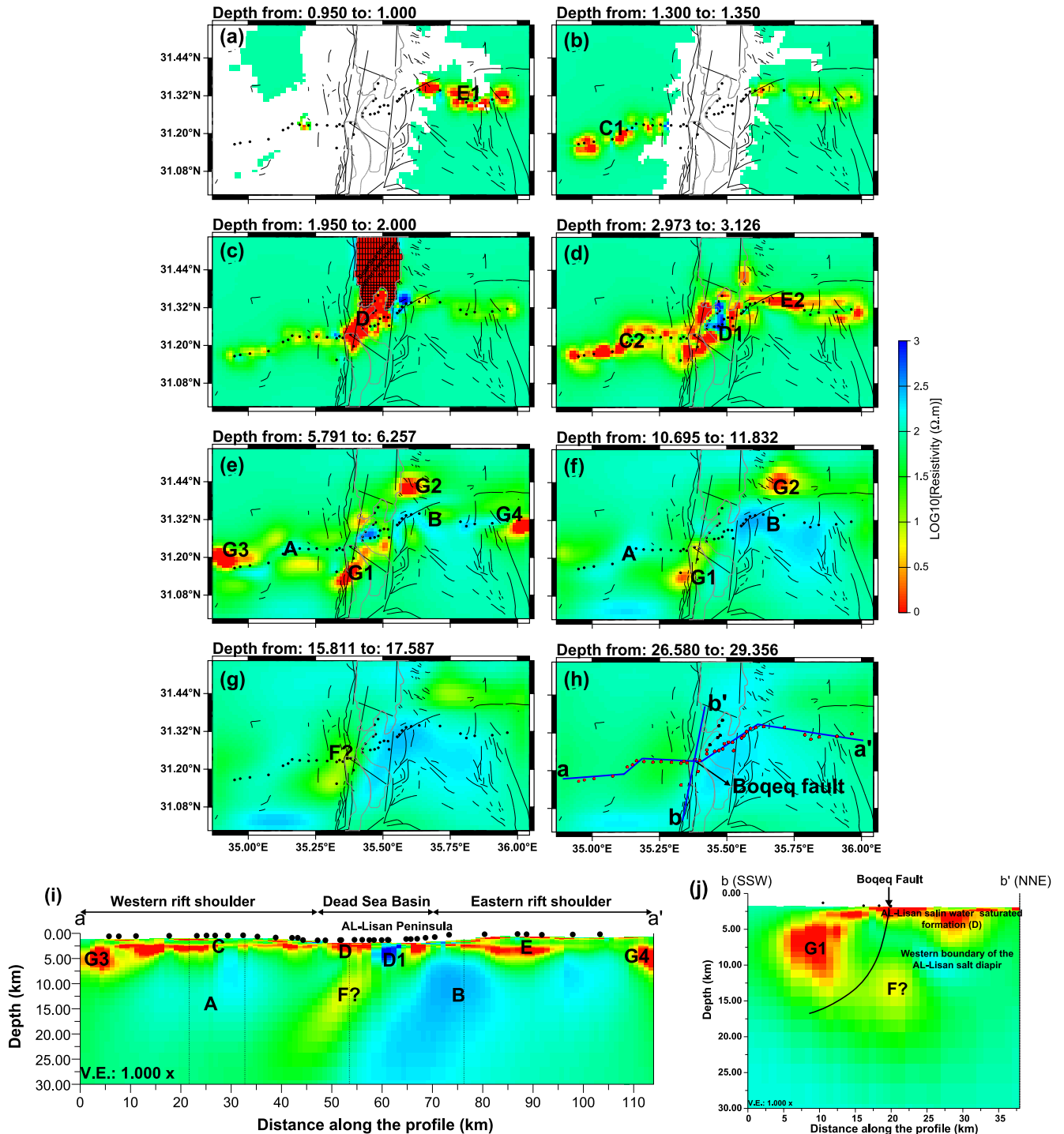


Figure 12. (a)–(h) 3-D inversion results shown in map view for a range of depths from upper to lower crustal levels. (i) and (j) are cross-sections extracted from the 3-D model along the main and in-basin profiles; see (h) for locations. The on-profile structures are labelled analogous to the 2-D model in Fig. 5(a), off-profile features are labelled G1–G4. Grey lines indicate fault traces and also the present outline of the Dead Sea. Dashed black line in (i) indicates positions where the section along the main profile changes direction. The depth extend of the surface footprint of the Boqeq fault in (j) is redrawn after Ben-Avraham & Schubert (2006).

Al-Zoubi & ten Brink 2002; Ben-Avraham & Schubert 2006; Smit *et al.* 2008) and density models (e.g. Choi *et al.* 2011).

At depths between ~ 5 and ~ 12 km, several off-profile features appear in the 3-D inversion model (labelled G1–G4 in Figs 12e and f). The most striking features are conductors labelled G1 and G2. G1 is located at the southern end of the in-basin profile which

covers the southern part of the Dead Sea. G1 appears to be limited in its horizontal dimensions, but reaches depths of approximately 12 km with resistivities ranging between 1 and $20 \Omega \text{ m}$ (Fig. 13b).

Tectonically, the Al-Lisan Peninsula is delimited by the En Geddi and Boqeq normal faults to the north and south, respectively (Fig. 1;

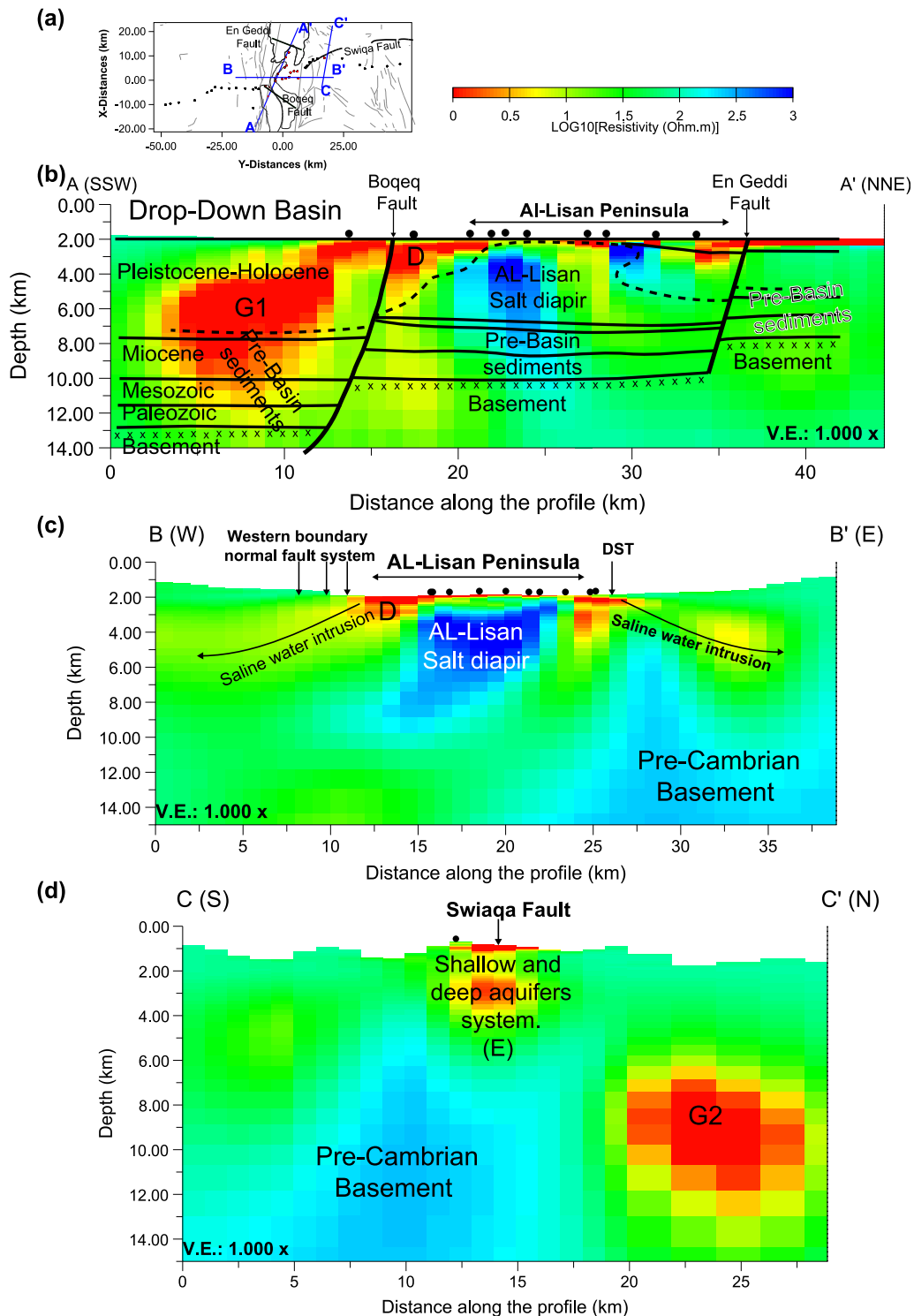


Figure 13. Three cross-sections extracted from the 3-D preferred model in Fig. 12 to investigate off-profile features G1 and G2 (b) and (d) as well as the Al-Lisan salt diapir (b) and (c). (a) Location map and surface traces of the En Geddi, Boqe and Swiaqa faults. The black outlines in (b) mark main geological features, redrawn after Ben-Avraham & Schubert (2006).

Ben-Avraham & Schubert 2006; Ben-Avraham *et al.* 2008). Salt diapirism forms the Al-Lisan Peninsula, a local topographical high, and the upwelling is likely caused by high subsidence rates of the DSB sediments (Al-Zoubi & ten Brink 2002; Al-Zoubi & Avraham 2002; Ten Brink & Flores 2012). As can be expected for massive

rock salt, the salt diapir is expressed as highly resistive material in the 3-D inversion model (Figs 13b and c).

Based on results from Ginzburg & Ben-Avraham (1997) and Al-Zoubi & Avraham (2002) using borehole stratigraphy and density models, Ben-Avraham & Schubert (2006) suggested a sedimentary

thickness of 6–8 km for the northern sub-basin. They also describe the Boqeq fault, as a major SE–NW oriented normal fault south of the Al-Lisan Peninsula. Across the Boqeq fault, basement and overlying sediments are ‘dropped-down’ by approximately 4–5 km to the south. Ben-Avraham & Schubert (2006) therefore describe the southern sub-basin of the DSB as a drop-down rather than a pull-apart basin. Fig. 13(b) suggests that the Boqeq fault also separates resistive structures of the Al-Lisan salt diapir from conductive structures further south. The top of the Al-Lisan salt diapir (dashed black line in Fig. 13b) correlates in general with the bottom of the very high conductive structures of the Al-Lisan sedimentary formations (D), which are likely brine saturated (Meqbel *et al.* 2013). It is therefore possible, that the very high conductivities observed for G1 at depth are also caused by invasion of Dead Sea brines into the deeper sedimentary formations.

Conductive feature labelled G2 which is located to the north of the main profile at the eastern rift shoulder is required to fit the **Tz** data. Southward rotating IVs at periods > 10 s (Fig. 3) also indicate a conductivity contrast located north of the eastern rift shoulder. Unfortunately, however, G2 appears at a location without MT site coverage. Fig. 13(d) shows a north–south trending cross-section extracted from the 3-D inversion model which crosses the Swiaqa fault (Fig. 1b). The Swiaqa fault is a major EW trending wrench fault which rotates south-westwards near the Dead Sea (Khalil 1992; Masri 2003, see Fig. 13a). The fault extends for ~150 km from the Dead Sea to the Sirhan graben near the Saudi Arabia border. The fault appears to have been reactivated several times over the last 5 Myr. (Khalil 1992) and resembles a major zone of weakness in the basement. A basalt intrusion is exposed at its western end. It is remarkable that the surface trace of the Swiaqa fault coincides with a transition at mid-crustal levels from resistive Pre-Cambrian basement in the south to conductive anomaly G2 to the north (Fig. 13d).

Conductive features G3 and G4 are located towards the western and eastern ends of the main profile. In cross-section view (Fig. 12i), G3 and G4 appear to be part (or extensions) of layers E and C. Obviously though, these features appear at the outer edges of the main profile where we lose resolution and where boundary effects may also play a role. The general trend of G3 would be consistent, however, with a suggested dip towards greater depths (Stanislavsky & Gvirtzman 1999).

Following the main profile, at depths between ~6 and ~20 km, the eastern rift shoulder is dominated by resistive structures (>500 Ω m), labelled B in Figs 12(f) and (i). For depths > 6 km, the western rift shoulder is also associated with higher resistivity material (labelled A in Figs 12f and i) but less pronounced when compared with the eastern rift shoulder. In the preferred 2-D inverse model (Fig. 5), the deeper parts of both rift shoulders were also imaged as resistive features but with much higher resistivity values (> 1000 Ω m). The depths to the tops of resistive blocks A and B appear to coincide with the top of the crystalline Pre-Cambrian rocks, in good agreement with seismic velocity models (Mechie *et al.* 2009) borehole data (Gilboa *et al.* 1993) and the 2-D MT results.

Between depths of 10 and 20 km, we observe region F with higher conductivity, sandwiched between the more resistive blocks A and B (see Figs 12g, i and j). The N–S cross-section in Fig. 12j shows that the two conductive features F and G1 are spatially separated. The conductive feature F is also disconnected from the overlying highly conductive (brine saturated) Al-Lisan sedimentary formations (D). The cross-sections in Figs 12(j) and 13(b) suggests furthermore that the southward dipping Boqeq normal fault could separate anomalies

G1 and F; the location of the fault plane was taken from Ben-Avraham & Schubert (2006).

Conductor F and its separation from G1 are required to fit the vertical magnetic field transfer functions (**Tz**). G1 appears only with the combined inversion approach which puts more weight on the **Tz** data than the standard inversion (see above). Nevertheless, compared to the **Tz**-only inversion, the lateral conductivity contrast between features A, F and B is expressed much weaker in the preferred model. To test the robustness of the conductive feature F in the preferred model we conducted several resolution studies.

A comparison between the cross-section along the main profile, extracted from the 3-D model (Fig. 12i), and the 2-D model (Fig. 5) shows that the uppermost crust to a depth of ~5 km appears similar in both. The deeper structures (> 5 km) differ; particularly conductivity contrasts appear much stronger in 2-D than in 3-D. From a numerical perspective, solving the 3-D inverse problem with data acquired along a profile results in a highly underdetermined problem, with a large number of unknown model parameters that must be projected onto the model space. The diffusive nature of the MT method results in high sensitivities for the shallow part of the model. Apparently, the 3-D inversion introduces shallow off-profile features at the cost of levelling out conductivity contrasts for deeper structures beneath the profile. To overcome this problem, it may be possible to impose constraints in the model domain where no MT sites are available. The best way, however, would be having more data from additional MT sites to control the horizontal extend and conductivity contrasts off-profile.

To examine the influence of off-profile structures on the 2-D inversion results, we generated synthetic data from the preferred 3-D model. Similarly to the real data, we then rotated the synthetic data into the geoelectrical strike direction of N12°E (see Fig. 2 and related discussion) and applied the same inversion settings as used to obtain the 2-D model presented in Fig. 5. Fig. 14 shows the 2-D inverse model and the corresponding nRMS values. Comparison between Figs 5 and 14 shows to some extent similar structures for the top most 5 km. The deeper structures (> 5 km) of the model in Fig. 14(a) are dominated by conductive structure labelled F, which appears directly underneath the DSB at depths between ~18 and ~50 km. The resistivity values of feature F vary between 2 and 10 Ω m. The 3-D model (Fig. 12), from which we generated the data, does not contain such a conductivity contrast. Very likely, such phantom structure at depth appear in the 2-D inversion model to accommodate for (shallow) off-profile features, such as G1 located to the south of the profile and the Dead Sea brines to the north. G2 (see Figs 12e and f) may be responsible for the appearance of conductive structures (≥ 10 Ω m) which interrupt the resistive Pre-Cambrian strata of the eastern rift shoulder.

We conducted further tests to examine the sensitivity of the field layout (i.e. site distribution) towards changes in the model parameters, particularly with respect to conductive feature F revealed from the 2-D modelling (e.g. Fig. 5). We altered the preferred 3-D model (Fig. 12) to include structures mimicking feature F with resistivity values of 1 Ω m and a strike in N–S direction, that is, 2-D structures (Fig. 15a). The horizontal extension of the included conductive feature was ~15 km in *y*-direction. We computed responses for two different site distributions: (i) the real site distribution (blue dots in Fig. 15d) and (ii) an ideal site distribution on a quasi-regular 2-D grid with a spacing of 2.5 km (black dots in Fig. 15d), in addition to the real site distribution. The model responses were computed using the period layout of the preferred 3-D inversion model and we assigned error floors of 5 per cent of $\sqrt{|Z_{xy}Z_{yx}|}$ to the four complex

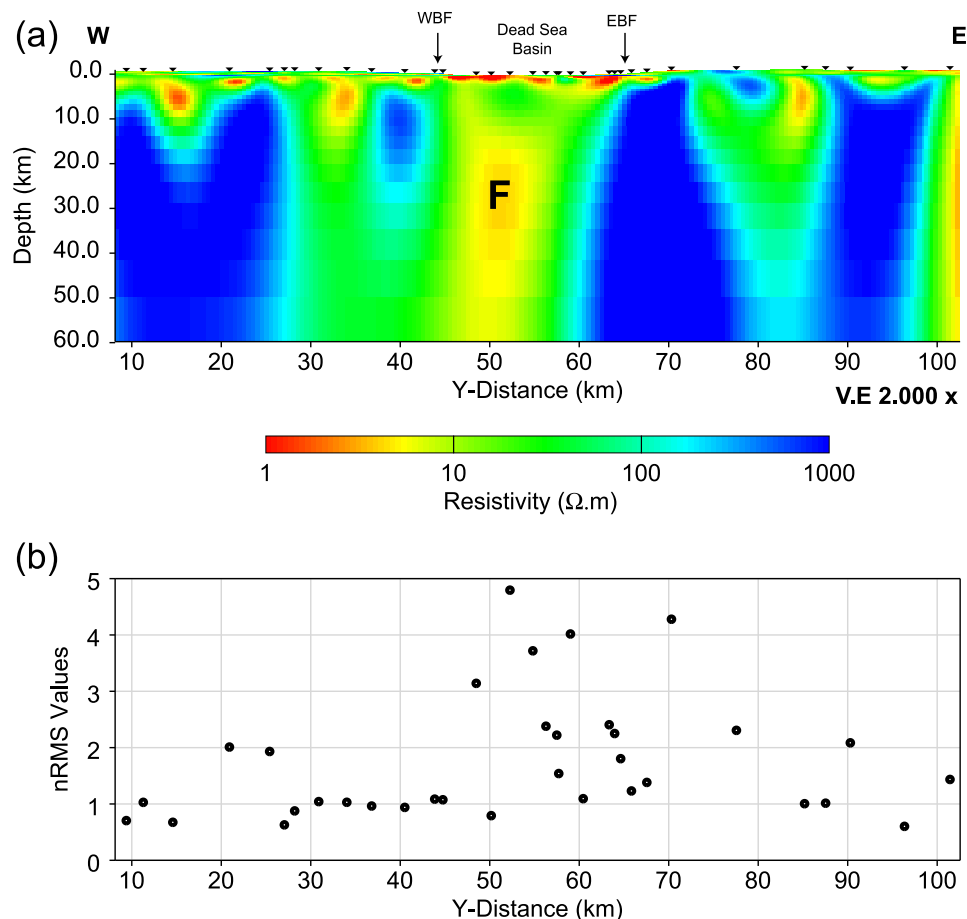


Figure 14. (a) The 2-D model obtained after inverting the predicted data of the preferred 3-D model in Fig. 12. (b) shows the corresponding data misfits as normalized RMS values at each station along the main profile. The 2-D model in (a) shows elevated resistivity values as depths > 5 km, much higher than in the underlying 3-D model (Fig. 12). Off-profile feature G1 (Fig. 13b) in combination with the Dead Sea brines may be responsible for the appearance of highly conductive feature F in the 2-D inversion model.

impedance tensor components of the predicted data. A constant value of 0.03 was used as error floor for the vertical magnetic field components.

Fig. 15(b) shows the inversion results of the synthetic data but using the real site distribution. Obviously, with the real site distribution, mostly following a profile, the 3-D inversion fails to recover the massive conductive channel, labelled $1 \Omega \text{ m}$ in Fig. 15(a). Structures in the upper ~ 5 km are generally well recovered, except for the highly resistive structures associated with the Al-Lisan Peninsula. When using the ideal data set computed on a regular 2-D grid (Fig. 15c) the 3-D inversion recovers the deep conductive channel, but its top appears smeared with the overlaying conductive sedimentary formation of the southern DSB (G1). In summary, with the site coverage used for the field experiment we neither can confirm nor exclude the existence of a deep, subvertical conductive structure (feature F) underneath the basin. More MT data with a better areal site distribution would be required to solve the puzzle.

7 DISCUSSION AND CONCLUSIONS

2-D inversion results of MT data gathered along a transect across the DSB reveal a pronounced subvertical electrically conductive channel at mid- and lower-crustal levels underneath the DSB, where the DST fault forks into two fault strands (Araba and Jericho faults) forming one of the largest pull-apart basins of the world. FZC have

been observed along major strike-slips faults around the world using the MT technique. We can plausibly interpret the subvertical conductive channel imaged in our preferred 2-D model in terms of a FZC in the middle and lower crust caused by shear movements along the DST fault. We attribute the conductive material within the fault zone to: (i) an upward migration of deep (partly mantle derived) fluids, (ii) released fluids during middle- to low-grade metamorphism in the lower crust and (iii) hydrous minerals created during retrograde metamorphism in the middle and upper crust.

Geochemical and geothermal reservoir modelling conducted at several hot springs along the DST fault reveal signatures for mantle derived fluids. Surface heat flow values ($45\text{--}53 \text{ mW m}^{-2}$) observed in the vicinity of the DSB is consistent with middle- to low-grade metamorphisms in the lower crust and a retrograde metamorphism in the middle and upper crust. Thermomechanic modelling suggests the presence of shear deformation localized in a 20–40 km wide zone around the DST fault, with a resulting mechanically weak decoupling zone extending subvertically through the entire lithosphere (Sobolev *et al.* 2005). Thermomechanic simulations also suggest that the DSB can be considered as a classical pull-apart basin, assuming that the lithosphere was thermally eroded at about 20 Myr. and an uppermost mantle with relatively weak rheology, which would be consistent with lab data for wet olivine or pyroxenite (Petrunin *et al.* 2012). In addition, the low friction coefficients required to model the architecture of the DSB thermomechanically

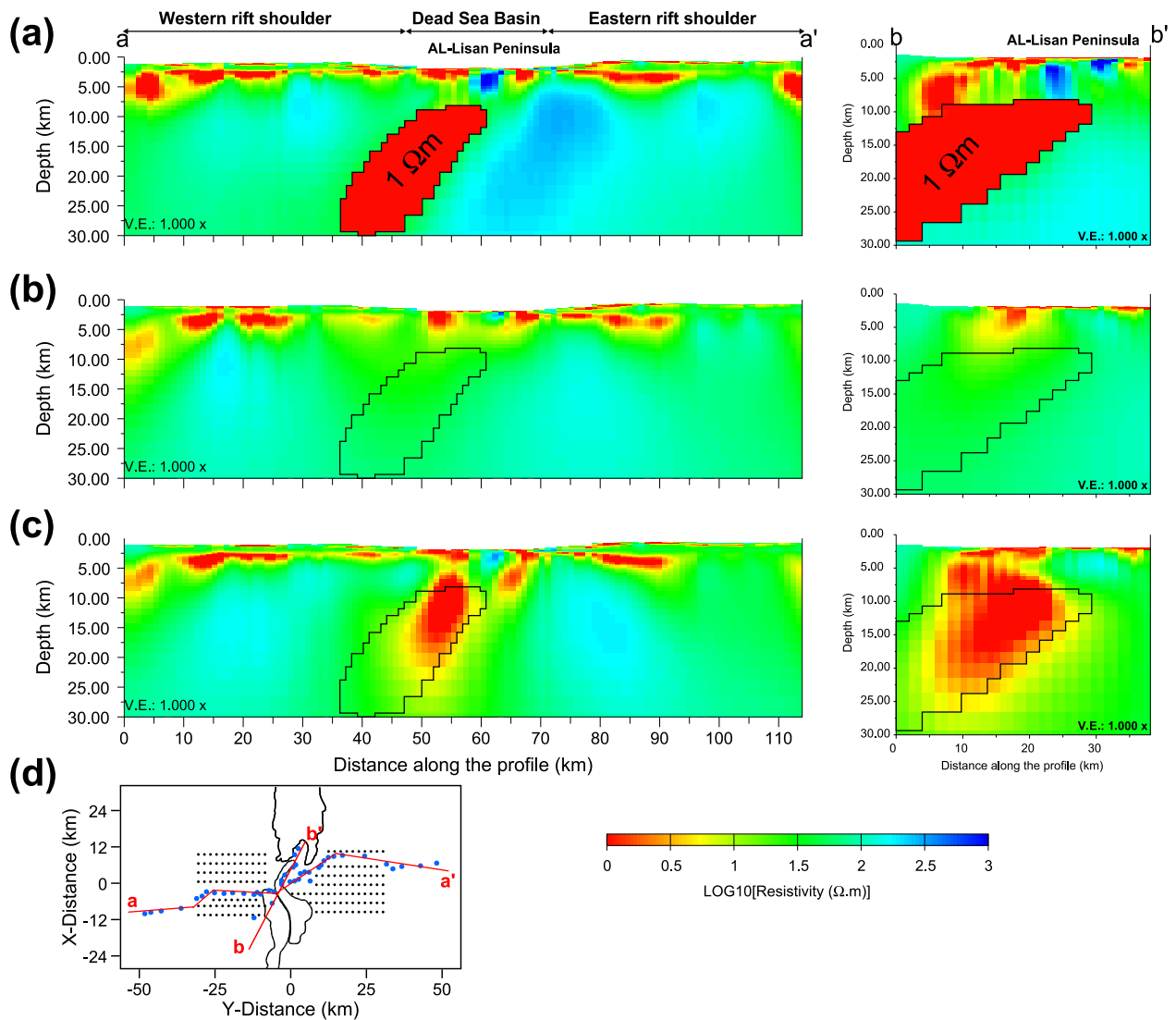


Figure 15. 3-D model appraisal to assess the sensitivity of the site layout with respect to changes in the subsurface resistivity structure. (a) We inserted a deep conductive channel, mimicking feature F, into our preferred 3-D model and created synthetic MT data. (b) The inversion of the synthetic data using the real site distribution (blue dots in (d)). (c) 3-D inversion result but now using a regular 2-D grid of sites distributed evenly around the Dead Sea Basin in addition to the real sites (black dots in d).

and the high subsidence rate of the basin sediments suggest the presence of hydrous minerals within the FZC.

In north–south direction, the DSB splits into sub-basins which are divided by a normal fault (Boqeq fault). Geophysical studies (gravity and seismics) conducted in and in the vicinity of the DSB suggest a sedimentary thickness of approximately 6–8 km for the northern sub-basin (Ten Brink *et al.* 1993; Choi *et al.* 2011). A southward drop-down along the Boqeq normal fault could result in deposition of an additional 4 km of sediments into the southern sub-basin (Ben-Avraham & Schubert 2006). The spatial distribution of the deep sedimentary formations in combination with the extremely conductive Dead Sea brines influence the outcome of the 3-D inversion, particularly the results along the main profile. The existence of a prominent sub-vertical conductor beneath the DSB remains enigmatic. There are strong hints that the depth extend and the extremely high conductivity revealed by the 2-D inversions are to a great extent influenced by the juxtaposed sedimentary forma-

tions which act as off-profile features which cannot be accounted for by 2-D modelling.

3-D modelling of quasi-profile data and in general is not straightforward and requires a considerable amount of attention. With the ‘combined joint inversion’ approach we could make better use of the information contained in the impedance tensor and VTFs, as standard 3-D inversion leads to models which mostly ignore structures required to fit the vertical magnetic fields. Nested modelling, inclusion of topography and fine discretization of the model space were all essential to derive geologically meaningful models and a reasonable data fit. The upper crustal structures revealed in our preferred 3-D resistivity model are to great extent consistent with structures revealed by 2-D inversion. The main discrepancy between the 2-D and 3-D models is observed underneath the DSB. The 3-D inversion model shows a weak signature of a subvertical conductive channel which was dominating the 2-D inversion result. Instead, the 3-D inversion suggests a deepening of electrically conductive material

(sediments) off-profile towards the southern sub-basin. While this result could be geologically reasonable, this conductor appears in the 3-D inversion model where we have no site coverage. With the available sites, we can neither confirm nor exclude the existence of a deep reaching, subvertical conductive structure beneath the DSB. More MT data with a better areal site distribution would be required to address this important question.

ACKNOWLEDGEMENTS

The authors would like to thank the reviewer Stephan Thiel and the editor Mark E. Everett for their helpful comments.

We gratefully thank all people who helped collecting DESIRE-MT data in Jordan and Israel: Jana Börner, Romina Gehrman, Olaf Helwig, Juliane Hübert, Thomas Krings, Christian Mielke, Stefanie Musiol, Stefan Rettig, Manfred Schüler and Wenke Wilhelms (Germany). Khalil Abu-Ayyash, Khaldon Abu Hamideh, Darwish Jaser, Jamal Khataibeh, Issam Qabbani, Husam Al-Rashdan and Tahsin Tal' at (Jordan). Yossi Bartov, Uri Frieslander and Gabby Heim (Israel).

This research was supported by the German Science Foundation (DFG) and the Helmholtz Centre Potsdam GFZ German Research Centre for Geosciences. Instruments for the MT measurements were provided by the Geophysical Instrument Pool Potsdam.

We thank the Natural Resources Authority of Jordan, the An-Najah University in Nablus, the Palestine Territories and the National Ministry of Infrastructure of Israel for their support throughout this project. We thank the military, security and customs agencies of Jordan and Israel for their help.

REFERENCES

- Al-Zoubi, A. & Avraham, Z.B., 2002. Structure of the Earth's crust in Jordan from potential field data, *Tectonophysics*, **346**(1–2), 45–59.
- Al-Zoubi, A. & ten Brink, U., 2002. Lower crustal flow and the role of shear in basin subsidence: an example from the Dead Sea basin, *Earth planet. Sci. Lett.*, **199**(1–2), 67–79.
- Aldersons, F., Ben-Avraham, Z., Hofstetter, A., Kissling, E. & Al-Yazjeen, T., 2003. Lower-crustal strength under the Dead Sea basin from local earthquake data and rheological modeling, *Earth planet. Sci. Lett.*, **214**(1–2), 129–142.
- Bahr, K., 1988. Interpretation of the magnetotelluric impedance tensor, regional induction and local telluric distortion, *J. Geophys.*, **62**, 119–127.
- Becken, M. & Burkhardt, H., 2004. An ellipticity criterion in magnetotelluric tensor analysis, *Geophys. J. Int.*, **159**(1), 69–82.
- Becken, M., Ritter, O., Bedrosian, P.A. & Weckmann, U., 2011. Correlation between deep fluids, tremor and creep along the central San Andreas fault, *Nature*, **480**(7375), 87–90.
- Ben-Avraham, Z. & Schubert, G., 2006. Deep “drop down” basin in the southern Dead Sea, *Earth planet. Sci. Lett.*, **251**(3–4), 254–263.
- Ben-Avraham, Z., Garfunkel, Z. & Lazar, M., 2008. Geology and evolution of the southern Dead Sea fault with emphasis on subsurface structure, *Annu. Rev. Earth Planet. Sci.*, **36**, 357–387.
- Boerner, D., Craven, J., Kurtz, R., Ross, G. & Jones, F., 1998. The Great Falls Tectonic Zone: suture or intracrustal shear zone?, *Can. J. Earth Sci.*, **35**(2), 175–183.
- Brauer, B., Asch, G., Hofstetter, R., Haberland, C., Jaser, D., El-Kelani, R. & Weber, M., 2012. Microseismicity distribution in the southern Dead Sea basin and its implications on the structure of the basin, *Geophys. J. Int.*, **188**(3), 873–878.
- Bruhnh, R.L., Yonkee, W.A. & Parry, W.T., 1990. Structural and fluid-chemical properties of seismogenic normal faults, *Tectonophysics*, **175**(1–3), 139–157.
- Caldwell, T.G., Bibby, H.M. & Brown, C., 2004. The magnetotelluric phase tensor, *Geophys. J. Int.*, **158**(2), 457–469.
- Choi, S., Götze, H.-J., Meyer, U. & DESIRE Group, 2011. 3-D density modelling of underground structures and spatial distribution of salt diapirism in the Dead Sea Basin, *Geophys. J. Int.*, **184**(3), 1131–1146.
- Desissa, M., Johnson, N.E., Whaler, K., Hautot, S., Fisseha, S. & Dawes, G., 2013. A mantle magma reservoir beneath an incipient mid-ocean ridge in Afar, Ethiopia, *Nat. Geosci.*, **6**(10), 861–865.
- Egbert, G.D., 1997. Robust multiple-station magnetotelluric data processing, *Geophys. J. Int.*, **130**(2), 475–496.
- Egbert, G.D. & Kelbert, A., 2012. Computational recipes for electromagnetic inverse problems, *Geophys. J. Int.*, **189**(1), 251–267.
- Eraifej, N., 2006. Gas geochemistry and isotopic signatures in the deep thermal waters in Jordan, *PhD thesis*, TU Bergakademie Freiberg.
- Etheridge, M.A., Wall, V.J. & Vernon, R.H., 1983. The role of the fluid phase during regional metamorphism and deformation, *J. Metamorph. Geol.*, **1**(3), 205–226.
- Friedman, G.M., Gvirtzman, H., Garven, G. & Gvirtzman, G., 1999. Thermal anomalies associated with forced and free ground-water convection in the Dead Sea rift valley: discussion and reply, *Bull. geol. Soc. Am.*, **111**(7), 1098–1102.
- Garfunkel, Z., 1981. Internal structure of the Dead Sea leaky transform (rift) in relation to plate kinematics, *Tectonophysics*, **80**(1–4), 81–108.
- Garfunkel, Z., Zak, I. & Freund, R., 1981. Active faulting in the Dead Sea rift, *Tectonophysics*, **80**(1–4), 1–26.
- Gilboa, Y., Fligelman, H. & Derin, B., 1993. Zohar-Kidod-Haqanaim fields, Israel, eastern Mediterranean basin, in *Structural Traps*, Vol. 8, *Treatise of Petroleum Geology Atlas of Oil and Gas Fields*, pp. 129–152, eds Foster, N.H. & Beaumont, E.A., American Association of Petroleum Geologists.
- Ginzburg, A. & Ben-Avraham, Z., 1997. A seismic refraction study of the north basin of the Dead Sea, Israel, *Geophys. Res. Lett.*, **24**(16), 2063–2066.
- Jones, A., Ledo, J. & Ferguson, I.J., 2005. Electromagnetic images of the Trans-Hudson orogen: the North American Central Plains anomaly revealed, *Can. J. Earth Sci.*, **42**(4), 457–478.
- Kafri, U. & Goldman, M., 2005. The use of the time domain electromagnetic method to delineate saline groundwater in granular and carbonate aquifers and to evaluate their porosity, *J. appl. Geophys.*, **57**(3), 167–178.
- Kafri, U., Goldman, M. & Lang, B., 1997. Detection of subsurface brines, freshwater bodies and the interface configuration in-between by the time domain electromagnetic method in the Dead Sea Rift, Israel, *Environ. Geol.*, **31**(1–2), 42–49.
- Kelbert, A., Meqbel, N., Egbert, G.D. & Tandon, K., 2014. ModEM: a modular system for inversion of electromagnetic geophysical data, *Comput. Geosci.*, **66**(0), 40–53.
- Kennedy, B.M., Kharaka, Y.K., Evans, W.C., Ellwood, A., DePaolo, D.J., Thorsen, J., Ambats, G. & Mariner, R., 1997. Mantle fluids in the San Andreas Fault system, California, *Science*, **278**(5341), 1278–1281.
- Khalil, B., 1992. The geology of the Ar Rabba area. Geological Map Bulletin No. 22, Natural Resource Authority (Jordan), Amman, Jordan.
- Klinger, Y., Avouac, J.P., Abou Karaki, N., Dorbath, L., Bourles, D. & Reyss, J.L., 2000. Slip rate on the Dead Sea transform fault in northern Araba valley (Jordan), *Geophys. J. Int.*, **142**(3), 755–768.
- Krings, T., 2007. The influence of robust statistics, remote reference, and horizontal magnetic transfer functions on data processing in magnetotellurics, *Master's thesis*, Institut fuer Geophysik stfaealische Wilhelms-Universitaet Muenster and GeoForschungsZentrum Potsdam.
- Leloup, P.H., Ricard, Y., Battaglia, J. & Lacassin, R., 1999. Shear heating in continental strike-slip shear zones: model and field examples, *Geophys. J. Int.*, **136**(1), 19–40.
- Masri, A., 2003. The geology of Dhiban (Wadi Al Mujib) area. Geological Map Bulletin No. 54, Natural Resource Authority (Jordan), Amman, Jordan.
- Mechie, J., Abu-Ayyash, K., Ben-Avraham, Z., El-Kelani, R., Qabbani, I., Weber, M. & DESIRE Group, 2009. Crustal structure of the southern Dead Sea basin derived from project DESIRE wide-angle seismic data, *Geophys. J. Int.*, **178**(1), 457–478.

- Meqbel, N.M., Egbert, G.D., Wannamaker, P.E., Kelbert, A. & Schultz, A., 2014. Deep electrical resistivity structure of the northwestern U.S. derived from 3-D inversion of USArray magnetotelluric data, *Earth planet. Sci. Lett.*, **402**, 290–304.
- Meqbel, N.M., 2009. The electrical conductivity structure of the Dead Sea Basin derived from 2D and 3D inversion of magnetotelluric data, *PhD thesis*, Free University of Berlin.
- Meqbel, N.M.M., Ritter, O. & DESIRE Group, 2013. A magnetotelluric transect across the Dead Sea Basin: electrical properties of geological and hydrological units of the upper crust, *Geophys. J. Int.*, **193**(3), 1415–1431.
- Neev, D. & Hall, J.K., 1979. Geophysical investigations in the Dead Sea, *Sediment. Geol.*, **23**(1–4), 209–238.
- Petrinin, A. & Sobolev, S., 2008. Three-dimensional numerical models of the evolution of pull-apart basins, *Phys. Earth planet. Inter.*, **171**(1–4), 387–399.
- Petrinin, A.G., Meneses Rioseco, E., Sobolev, S.V. & Weber, M., 2012. Thermomechanical model reconciles contradictory geophysical observations at the Dead Sea Basin, *Geochem. Geophys. Geosyst.*, **13**(4), doi:10.1029/2011GC003929.
- Ritter, O., Junge, A. & Dawes, G. J.K., 1998. New equipment and processing for magnetotelluric remote reference observations, *Geophys. J. Int.*, **132**, 535–548.
- Ritter, O., Ryberg, T., Weckmann, U., Hoffmann-Rothe, A., Abueladas, A., Garfunkel, Z. & DESERT Research Group, 2003. Geophysical images of the Dead Sea Transform in Jordan reveal an impermeable barrier for fluid flow, *Geophys. Res. Lett.*, **30**(14), doi:10.1029/2003GL017541.
- Ritter, O., Hoffmann-Rothe, A., Bedrosian, P.A., Weckmann, U. & Haak, V., 2005. Electrical conductivity images of active and fossil fault zones, *Geol. Soc., Lond., Spec. Publ.*, **245**(1), 165–186.
- Rodi, W. & Mackie, R.L., 2001. Nonlinear conjugate gradients algorithm for 2-D magnetotelluric inversion, *Geophysics*, **66**(1), 174–187.
- Salameh, E.E. & -Naser, H., 2000. The interface configuration of the Fresh-/Dead Sea water: theory and measurements, *Acta Hydroch. Hydrobiol.*, **28**(6), 323–328.
- Schaeffer, R. & Sass, I., 2014. The thermal springs of Jordan, *Environ. Earth Sci.*, **72**(1), 171–187.
- Siler, D.L. & Kennedy, B.M., 2016. Regional crustal-scale structures as conduits for deep geothermal upflow, *Geothermics*, **59**(Part A), 27–37.
- Smit, J., Brun, J.-P., Fort, X., Cloetingh, S. & Ben-Avraham, Z., 2008. Salt tectonics in pull-apart basins with application to the Dead Sea Basin, *Tectonophysics*, **449**(1–4), 1–16.
- Sobolev, S., Petrinin, A., Garfunkel, Z. & Babeyko, A., 2005. Thermo-mechanical model of the Dead Sea Transform, *Earth planet. Sci. Lett.*, **238**(1–2), 78–95.
- Stanislavsky, E. & Gvirtzman, H., 1999. Basin-scale migration of continental-rift brines: paleohydrologic modeling of the Dead Sea basin, *Geology*, **27**(9), 791–794.
- Tank, S.B. *et al.*, 2005. Magnetotelluric imaging of the fault rupture area of the 1999 Izmit (Turkey) earthquake, *Phys. Earth planet. Inter.*, **150**(1–3), 213–225.
- Ten Brink, U.S. & Flores, C.H., 2012. Geometry and subsidence history of the Dead Sea basin: a case for fluid-induced mid-crustal shear zone?, *J. geophys. Res.*, **117**, B01406, doi:10.1029/2011JB008711.
- Ten Brink, U.S., Ben-Avraham, Z., Bell, R.E., Hassouneh, M., Coleman, D.F., Andreassen, G., Tibor, G. & Coakley, B., 1993. Structure of the Dead Sea pull-apart basin from gravity analyses, *J. geophys. Res.*, **98**(B12), 21 877–21 894.
- Thiel, S., Heinson, G., Gray, D.R. & Gregory, R.T., 2009. Ophiolite emplacement in NE Oman: constraints from magnetotelluric sounding, *Geophys. J. Int.*, **176**(3), 753–766.
- Unsworth, M. & Bedrosian, P., 2004. On the geoelectric structure of major strike-slip faults and shear zones, *Earth Planets Space*, **56**(12), 1177–1184.
- Vozoff, K., 1991. The magnetotelluric method, in *Electromagnetic Methods in Applied Geophysics II*, Chap. 8, pp. 641–712, ed. Nabighian, M., Society of Exploration Geophysicists, Tulsa Oklahoma.
- Wannamaker, P.E., 2005. Anisotropy versus heterogeneity in continental solid earth electromagnetic studies: fundamental response characteristics and implications for physicochemical state, *Surv. Geophys.*, **26**(6), 733–765.
- Weaver, J.T., 1994. *Mathematical Methods for Geo-electromagnetic Induction*, Applied and Engineering Mathematic Series, Research Studies Press, Taunton, Somerset, England.
- Weber, M. *et al.*, 2009. Anatomy of the Dead Sea Transform from lithospheric to microscopic scale, *Rev. Geophys.*, **47**(2), doi:10.1029/2008RG000264.
- Weber, M. *et al.*, 2011. Results of geophysical studies across the Dead Sea Transform: The Arava/Araba Valley and the Dead Sea Basin, *Isr. J. Earth-Sci.*, **58**, 147–161.
- Weckmann, U., Magunia, A. & Ritter, O., 2005. Effective noise separation for magnetotelluric single site data processing using a frequency domain selection scheme, *Geophys. J. Int.*, **161**, 635–652.
- Wiese, H., 1962. Geomagnetische Tiefentellurik Teil II: Die Streichrichtung der Untergrundstrukturen des elektrischen Widerstandes, erschlossen aus geomagnetischen Variationen, *Geofis. Pura Appl.*, **52**(1), 83–103.
- Yechieli, Y., 2006. Response of the groundwater system to changes in the Dead Sea level, *Geol. Soc. Am. Spec. Papers*, **401**, 113–126.
- Yechieli, Y., Kafri, U., Goldman, M. & Voss, C., 2001. Factors controlling the configuration of the fresh-saline water interface in the Dead Sea coastal aquifers: synthesis of TDEM surveys and numerical groundwater modeling, *Hydrogeol. J.*, **9**(4), 367–377.
- Zak, I. & Freund, R., 1981. Asymmetry and basin migration in the Dead Sea rift, *Tectonophysics*, **80**(1–4), 27–38.